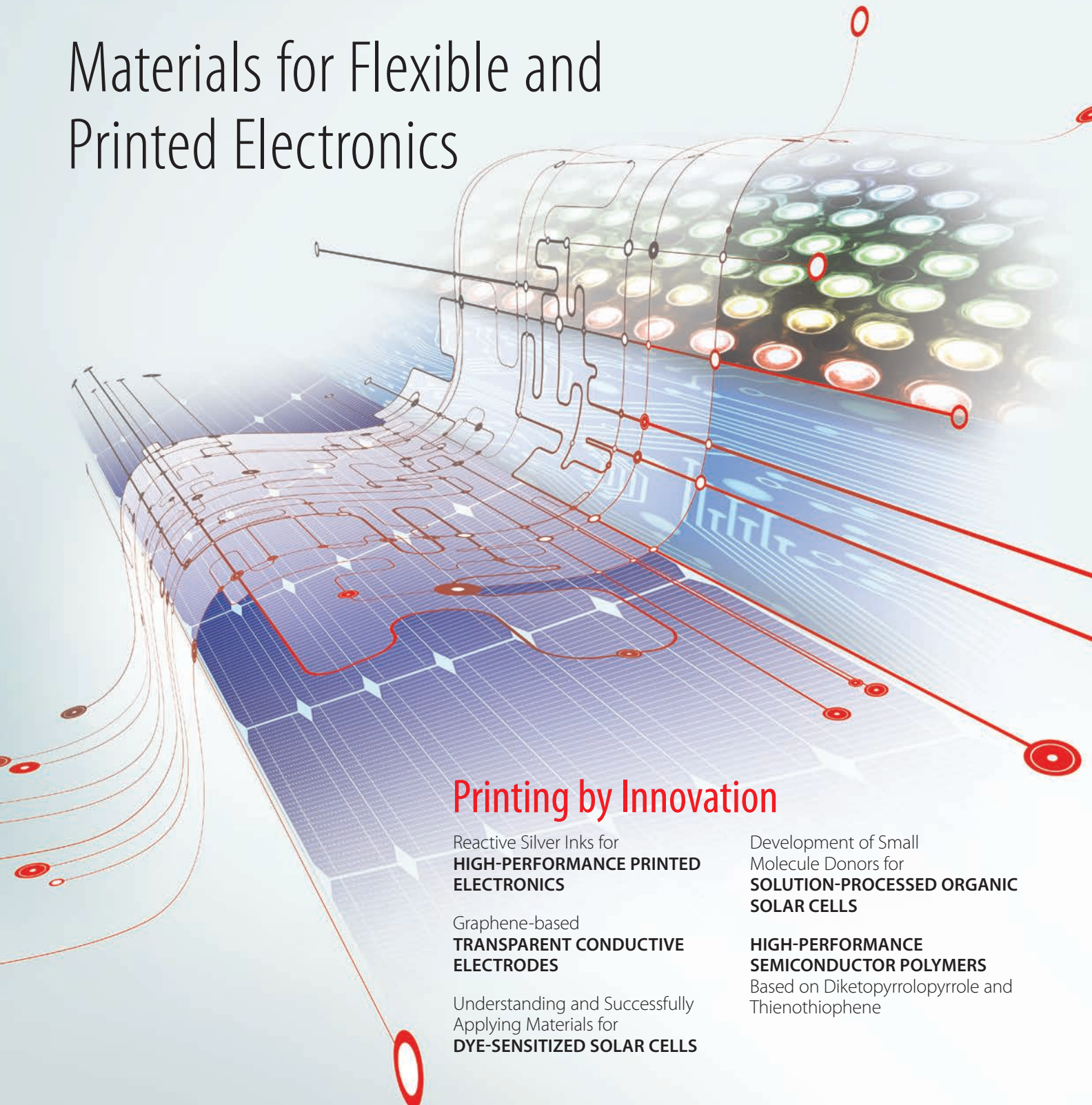


# Material Matters™

Volume 9, Number 1

**ALDRICH**  
Materials Science

## Materials for Flexible and Printed Electronics



### Printing by Innovation

Reactive Silver Inks for  
**HIGH-PERFORMANCE PRINTED ELECTRONICS**

Graphene-based  
**TRANSPARENT CONDUCTIVE ELECTRODES**

Understanding and Successfully Applying Materials for  
**DYE-SENSITIZED SOLAR CELLS**

Development of Small Molecule Donors for  
**SOLUTION-PROCESSED ORGANIC SOLAR CELLS**

**HIGH-PERFORMANCE SEMICONDUCTOR POLYMERS**  
Based on Diketopyrrolopyrrole and Thienothiophene

## Introduction

Welcome to the first issue of *Material Matters*™ for 2014, focusing on *Materials for Flexible and Printed Electronics*. Flexible and Printed Electronics includes a broad set of technologies applicable from very small electronic devices to large-area electronics across a great number of products. Innovation on printing techniques makes high throughput and volume production of electronics possible at low cost on flexible plastic, paper, or textile substrates. This flexibility will enable integration of printed and flexible electronics into everyday items and places we had only dreamed of before.

Functional materials have been developed and optimized for various printing methods, including ink-jet, gravure, flexographic, and offset printing. Printing electronic components such as displays, photovoltaic panels, RFID tags, and others require conductive and/or semiconductive materials. Conductive inks can be metal or conducting polymers-based. Semiconductive materials can be based on semiconducting polymers, small organic molecules, and carbon nanomaterials. This issue concentrates on inorganic metallic conducting materials (particularly silver) and organic electronics materials including carbon nanomaterials, small organic materials, and polymers, where recent flexible and printed electronics research has been focused.

The first article, by S. Brett Walker, Bok Yeop Ahn, and Jennifer A. Lewis (USA), describes reactive silver inks that can be used as electrodes in high-performance printed electronics. Silver electrodes have been patterned on low-cost polymer substrates by inkjet printing the reactive silver ink. Through chemical modification, the ink viscosity and surface tension can be tuned (from 5–50 mPa·s and 20–50 mN/m, respectively) for optimized jetting, while achieving high electrical conductivity at modest temperatures (~100 °C).

Kehan Yu and Junhong Chen (USA) in the second article provide a summary of recent graphene-based transparent conductive electrodes (TCEs) from theory to application. They discuss the advantages and disadvantages of each graphene preparation technique (solution process vs. CVD growth). Graphene-based hybrid TCEs made by combining graphene and other nanomaterials (e.g., carbon nanotubes as a conductive filler) are highlighted, emphasizing their excellent performance.

In the third article, Hans Desilvestro, Yanek Hebling, Mikael Khan, and Damion Milliken (Australia) review key materials such as titania semiconductors, ruthenium-based dyes, electrolytes, platinum catalysts, and silver conductors for successful assembly of dye-sensitized solar cell (DSC) devices. This review provides a detailed account of the interactions between the materials and their significant parameters.

The fourth article, by Abby-Jo Payne and Gregory C. Welch (Canada), highlights the transition from polymers to small molecule-based organic solar cells over the last few years and reviews key structural features that have led to this paradigm shift. Small molecules offer advantages over their polymeric counterparts for use in photovoltaics in that structures are well-defined and lead to improved purity and no molecular weight dependence, thus limiting batch-to-batch variation. Additionally, electronic energy levels, optical absorption, and self-assembly tendencies can be way more systematically tuned from small molecules to maximize device performance.

Finally, Tony Wigglesworth, Yiliang Wu, Cuong Vong, and Matthew Heuft (Canada) describe the applications of diketopyrrolopyrrole–thienothiophene (DPP–TT) copolymers in solution-processed OFET devices. DPP–TT copolymers are one of the most promising semiconductor materials for applications in printed electronics due to their outstanding solution processability and aggregation properties provided by strong donor–acceptor interactions.

Each article in this issue is accompanied by a list of relevant materials available from Aldrich® Materials Science to facilitate fabrication of high-performance electronic devices. For additional product and technical information, visit us at [aldrich.com/matsci](http://aldrich.com/matsci). Send your comments/suggestions for *Material Matters*, or your product suggestions, to [matsci@sial.com](mailto:matsci@sial.com).

You'll notice that we've improved *Material Matters* with a more reader-friendly design that makes it easier to find the products and resources you need. We look forward to continuing to bring you the expert articles you expect in a format that quickly connects you with the world-class tools your work demands.

## About Our Cover

Flexible and Printed Electronics is a cutting-edge technology that promises to enable a variety of creative applications in electronics by combining functional materials with traditional printing techniques. The cover art expresses an ideal device comprised of flexible, printed components in which electricity converted from printed solar panels powers flexible displays through printed circuits. Aldrich Materials Science is proud to serve researchers in these areas with a large variety of innovative materials.



Jia Choi, Ph.D.  
Aldrich Materials Science

# Material Matters™

Vol. 9, No. 1

**Aldrich Materials Science**  
**Sigma-Aldrich Co. LLC**  
6000 N. Teutonia Ave.  
Milwaukee, WI 53209, USA

### To Place Orders

Telephone 800-325-3010 (USA)  
FAX 800-325-5052 (USA)

International customers, contact your local Sigma-Aldrich office ([sigma-aldrich.com/worldwide-offices](http://sigma-aldrich.com/worldwide-offices)).

### Customer & Technical Services

Customer Inquiries 800-325-3010  
Technical Service 800-325-5832  
SAFC® 800-244-1173  
Custom Synthesis 800-244-1173  
Flavors & Fragrances 800-227-4563  
International 314-771-5765  
24-Hour Emergency 314-776-6555  
Safety Information [sigma-aldrich.com/safetycenter](http://sigma-aldrich.com/safetycenter)  
Website [sigma-aldrich.com](http://sigma-aldrich.com)  
Email [aldrich@sial.com](mailto:aldrich@sial.com)

### Subscriptions

Request your FREE subscription to *Material Matters*:

Phone 800-325-3010 (USA)  
Mail Attn: Marketing Communications  
Aldrich Chemical Co., Inc  
Sigma-Aldrich Co. LLC  
P.O. Box 2060  
Milwaukee, WI 53201-2060  
Website [aldrich.com/mm](http://aldrich.com/mm)  
Email [sams-usa@sial.com](mailto:sams-usa@sial.com)

*Material Matters* (ISSN 1933–9631) is a publication of Aldrich Chemical Co., Inc. Aldrich is a member of the Sigma-Aldrich Group.

### Online Versions



Explore previous editions of *Material Matters*. Visit [aldrich.com/materialmatters](http://aldrich.com/materialmatters)



Now available for your iPad®  
[aldrich.com/mm](http://aldrich.com/mm)

©2014 Sigma-Aldrich Co. LLC. All rights reserved. SIGMA, SAFC, SIGMA-ALDRICH, ALDRICH, SUPELCO, and SAFC Hitech are trademarks of Sigma-Aldrich Co. LLC, registered in the US and other countries. FLUKA is a trademark of Sigma-Aldrich GmbH, registered in the US and other countries. Material Matters is a trademark of Sigma-Aldrich Co. LLC. Dyesol is a registered trademark of Dyesol Ltd. iPad is a registered trademark of Apple Inc. CoMoCAT and V2V are trademarks of SouthWest NanoTechnologies, Inc. IsoNanotubes-M, IsoNanotubes-S, PureTubes, and SuperPureTubes are trademarks of Nanolntegrals, Inc. Orgacon is a trademark of Agfa-Gevaert N.V. Plexcore is a registered trademark of Plextronics, Inc. Rieke is a registered trademark of Rieke Metals, Inc. SWeNT is a registered trademark of SouthWest NanoTechnologies, Inc. Xerox is a registered trademark of Xerox Corporation. Sigma brand products are sold through Sigma-Aldrich, Inc. Purchaser must determine the suitability of the product(s) for their particular use. Additional terms and conditions may apply. Please see product information on the Sigma-Aldrich website at [www.sigmaaldrich.com](http://www.sigmaaldrich.com) and/or on the reverse side of the invoice or packing slip.

# Table of Contents

## Articles

Reactive Silver Inks for High-performance Printed Electronics	2
Graphene-based Transparent Conductive Electrodes	6
Understanding and Successfully Applying Materials for Dye-sensitized Solar Cells	14
Development of Small Molecule Donors for Solution-processed Organic Solar Cells	23
High-performance Semiconductor Polymers Based on Diketopyrrolopyrrole and Thienothiophene	33

## Featured Products

<b>Silver Inks and Dispersions</b> A selection of silver inks, nanoparticle and nanowire dispersions for printing	4
<b>Graphene and Graphene Oxide (GO)</b> A list of monolayer graphene films and graphene oxide dispersions	10
<b>Carbon Nanotubes (CNTs)</b> A list of CNTs and single-walled CTN inks	10
<b>Organic Conductive Inks and Ink Kits</b> A selection of organic conductive inks and ink kits for use in printed electronics	12
<b>Indium Tin Oxide (ITO) Coated Substrates</b> A list of ITO coated PET and glass substrates	13
<b>Fluorine-doped Tin Oxide (FTO) Coated Substrates</b> A list of FTO coated glass substrates	13
<b>Dyes</b> A selection of metal complex and metal-free dyes for use in dye-sensitized solar cells	18
<b>Nanoparticles</b> A selection of TiO <sub>2</sub> and ZnO nanoparticles for use in dye-sensitized solar cells	21
<b>Pastes</b> Silver, titania and platinum pastes for use in dye-sensitized solar cells	21
<b>Electrolytes</b> A selection of liquid electrolytes for use in dye-sensitized solar cells	22
<b>Organic Hole Conductors</b> A selection of organic hole transport materials for use in dye-sensitized solar cells	22
<b>P-type Small Molecules</b> A selection of p-type small molecular semiconductors for use in flexible electronics	28
<b>N-type Small Molecules</b> A selection of n-type small molecular semiconductors for use in flexible electronics	30
<b>Fullerenes</b> A selection of fullerene derivatives for use in flexible electronics	31
<b>P-type Polymers</b> A selection of p-type polymeric semiconductors for use in flexible electronics	34
<b>N-type Polymers</b> A selection of n-type polymeric semiconductors for use in flexible electronics	36

# Your Materials Matter



*Bryce P. Nelson*

Bryce P. Nelson, Ph.D.  
Aldrich Materials Science Initiative Lead

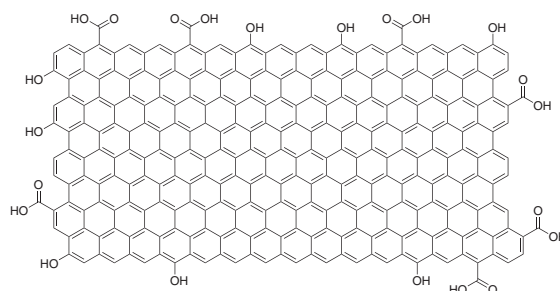
We welcome fresh product ideas. Do you have a material or compound you wish to see featured in the Aldrich® Materials Science line? If it is needed to accelerate your research, it matters. Send your suggestion to [matsci@sial.com](mailto:matsci@sial.com) for consideration.

Dr. Marja Viikman of VTT Technical Research Centre of Finland recommended the addition of reduced graphene oxide (rGO, **Aldrich Prod. No. 777684**) to our catalog as a material for flexible electronics. Inkjet printing is one of the most promising techniques for large-area fabrication of flexible plastic electronics. A range of components can be printed, such as transistors, photovoltaic devices, organic light-emitting diodes (OLEDs), and displays. Graphene products like rGO have significant potential for use in printed electronics due to their easy handling, superior electrical conductivity, stability, and printing versatility.<sup>1-3</sup>

## References

- (1) Grande, Lorenzo; Chundi, Vishnu Teja; Wei, Di; Bower, Chris; Andrew, Piers; Ryhänen, Tapani *Particology*, **2012**, *10*, 1-8.
- (2) Torrisi, Felice; Hasan, Tawfique; Wu, Weiping; Sun, Zhipei; Lombardo, Antonio; Kulmala, Tero S.; Hsieh, Gen-Wen; Jung, Sungjune; Bonaccorso, Francesco; Paul, Philip J.; Chu, Daping; Ferrari, Andrea C. *ACS Nano*, **2012**, *6*, 2992-3006.
- (3) Secor, Ethan B.; Prabhumirashi, Pradyumna L.; Puntambekar, Kanan; Geier, Michael L.; Hersam, Mark C. *J. Phys. Chem. Lett.*, **2013**, *4*, 1347-1351.

## Reduced graphene oxide



rGO  
C<sub>x</sub>O<sub>y</sub>H<sub>z</sub>

- Reduction method: Chemically reduced
- Color: Black
- Odor: Odorless
- Solubility: Insoluble
- Dispersability: It can be dispersed at low concentrations (<0.1 mg/mL) in NPM, DMSO, DMF
- Electrical conductivity: >600 S/m
- BET surface area: 450 m<sup>2</sup>/g

<a href="#">777684-250MG</a>	250 mg
<a href="#">777684-500MG</a>	500 mg

# REACTIVE SILVER INKS FOR HIGH-PERFORMANCE PRINTED ELECTRONICS



S. Brett Walker,<sup>1,2</sup> Bok Yeop Ahn,<sup>3\*</sup> Jennifer A. Lewis<sup>1,3,4</sup>

<sup>1</sup>Materials Science and Engineering Department  
University of Illinois at Urbana-Champaign, Urbana, IL 61801

<sup>2</sup>Electroninks Incorporated, Champaign, IL 61820

<sup>3</sup>Wyss Institute for Biologically Inspired Engineering, Harvard University, Cambridge, MA 02138

<sup>4</sup>Harvard School of Engineering and Applied Science, Cambridge, MA 02138

Email: jalewis@seas.harvard.edu

## Introduction

The ability to pattern conductive electrodes is technologically relevant for several applications, including photovoltaics,<sup>1</sup> displays,<sup>2</sup> sensors,<sup>3</sup> and biomedical devices.<sup>4</sup> Conductive silver electrodes are ubiquitous in such applications due to their high conductivity and oxidation resistance. Silver particle inks are widely used; however, they often require complicated synthesis routes,<sup>5</sup> relatively high polymer concentrations,<sup>6</sup> and must be annealed at high temperatures that are incompatible with most organic substrates. To overcome these limitations, silver precursor inks have been introduced that can be readily synthesized and exhibit high electrical conductivity at modest annealing temperatures.<sup>7-12</sup>

## Silver Precursor Inks

Three classes of silver precursor inks have been reported to date. One type relies on decarboxylation of a counterion or a thermally degradable carbamate complex that yields conductivities within one order of magnitude of bulk silver.<sup>8</sup> Another type relies on thermal activation of reducing agents above a threshold temperature.<sup>9</sup> Both of these inks require annealing temperatures in excess of 120 °C to achieve appreciable conductivity. Recently, we introduced a new type of ink, referred to as a reactive silver ink.<sup>10</sup> This ink was prepared by a modified Tollens' reagent synthesis using silver acetate, formic acid, and ammonia. While this ink exhibited high conductivity at temperatures as low as 90 °C, one drawback of this initial chemistry is significant gas evolution, i.e., bubble formation, that occurs during annealing. Another limitation arises from its low viscosity (2 mPa·s) and high surface tension (>60 mN/m), which makes inkjet printing quite challenging.

Inks designed for inkjet printing must meet stringent physical property requirements. The Ohnesorge (*Oh*) number (a dimensionless number that relates viscous forces to inertial and surface tension forces) must be within certain values for reliable jetting. *Oh* is given by:

$$Oh = \frac{\sqrt{We}}{Re}$$

where *We* is the Weber number and *Re* is the Reynolds number.<sup>11</sup> A value of 0.1 to 1 is generally accepted to be in the range of stable droplet formation. Derby<sup>11</sup> further reported that the minimum velocity (*u*<sub>min</sub>) required to generate droplets is given by:

$$u_{\min} = \sqrt{\frac{4\gamma}{\rho d_n}}$$

where,  $\gamma$ ,  $\rho$ , and  $d_n$  are the surface tension, density, and nozzle diameter, respectively. This minimum droplet velocity was difficult to obtain using the original silver reactive ink at the excitation voltages (<40 V) available on typical inkjet printing machines due to its low viscosity and high surface tension.

## Modified Reactive Silver Ink

Here, we report a modified reactive silver ink (**Aldrich Prod. No. 745707**) that incorporates a primary amine for optimized jetting. In its synthetic procedure, silver acetate is dissolved in an aqueous solution mixture of primary amine, propylene glycol, and other humectants. Formic acid (or ammonium formate) is then added to the resultant solution in an ice-cooled water bath, followed by syringe filtering by pore size of 0.2  $\mu\text{m}$ . **Figure 1A** shows the particle-free ink after synthesis. Unlike the clear ink formed without a primary amine, the modified ink appears slightly yellow due to the presence of the Ag-amine complex (**Figure 1B**). The UV-Vis spectrum shows the absorption in the region of 400–425 nm, indicating the reaction of silver and primary amine with formic acid (**Figure 1C**). This ink is relatively stable at room temperature and does not rapidly form silver particles until heated to 50–60 °C. **Figure 1D** shows the thermogravimetric analysis (TGA) data for inks heated at 80 °C, 100 °C, and 120 °C as a function of annealing time. These curves show that the ink contains approximately 13 wt% silver. Notably, the volatile constituents are completely removed within a few minutes at 120 °C, and bubble formation is not observed during annealing.

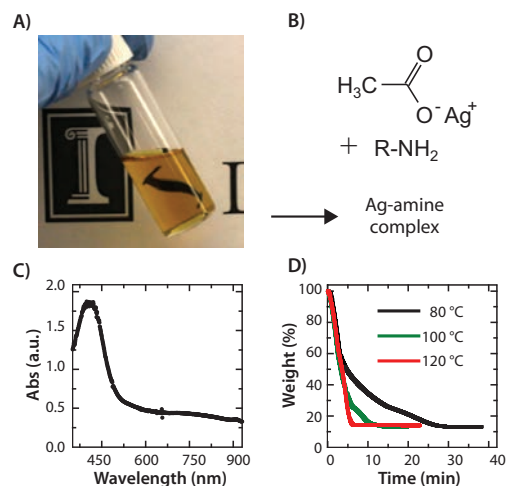


**Figure 1.** A) Image of the modified reactive Ag ink composed of 13 wt% solids. B) Illustration of the key ink constituents. C) UV-vis absorption of the ink. D) Thermogravimetric analysis of the ink measured at varying temperatures as a function of annealing time.

The viscosity of the modified reactive silver ink is 10 mPa·s, which represents a five-fold increase relative to the original ink formulation.<sup>10</sup> Furthermore, by incorporating alkyl amines with bulkier side groups, the ink viscosity and surface tension can be systematically tuned over a broad range from 5–50 mPa·s and 20–50 mN/m, respectively. This tunability enables our modified reactive silver inks to be formulated for myriad patterning techniques, including inkjet, spin-coating, aerosol, electrohydrodynamic jet, and roll-to-roll printing.

The time sequence of droplet formation achieved during inkjet printing using a Fuji Dimatix printer equipped with a 10 pL cartridge is shown in **Figure 2A**. The waveform and excitation voltage are selected to minimize the formation of satellite droplets, which diminish pattern fidelity.

**Figures 2B** and **C** show optical and SEM images of the silver electrodes patterned on a cellulose acetate substrate with a range of line widths from 80  $\mu\text{m}$  to 1.5 cm. By carefully choosing the appropriate alkylamine ligands, the modified reactive silver ink exhibits low surface tension, increased adhesion, and negligible bubble formation without the use of polymeric additives.

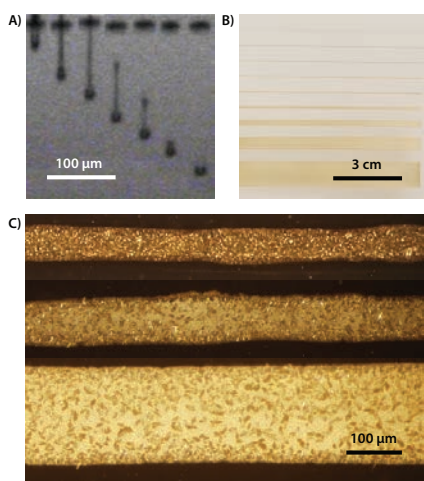


**Figure 2.** A) Image of droplet formation from a 10 pL cartridge with a 10  $\mu\text{s}$  interval between images. B) Image of conductive pattern produced on cellulose acetate after a single pass annealed at 100 °C for 2 min. C) Micrographs of the smallest lines (70  $\mu\text{m}$  top, 110  $\mu\text{m}$  middle, 180  $\mu\text{m}$  bottom) produced in B).

Microstructural evolution as a function of the number of printed layers is illustrated in **Figure 3A**. Single-pass, printed features are porous, conductive (~10% of bulk silver), and translucent. Their electrical conductivity increases by approximately 20% per pass, such that five-layer printed features exhibit nearly bulk conductivity (**Figure 3B**). The layer height remains relatively unchanged with an increasing number of passes (up to five passes). The SEM images reveal that as additional ink is deposited per pass, the patterned electrode structures densify as the excess silver fills in the underlying pores in a given area. After five layers have been deposited, the film height increases by approximately 350 nm. Hence, the layer height only grows after the porosity present within the patterned electrode features has been filled. By contrast, printed electrodes produced from silver nanoparticle inks remain porous even upon deposition of subsequent layers.

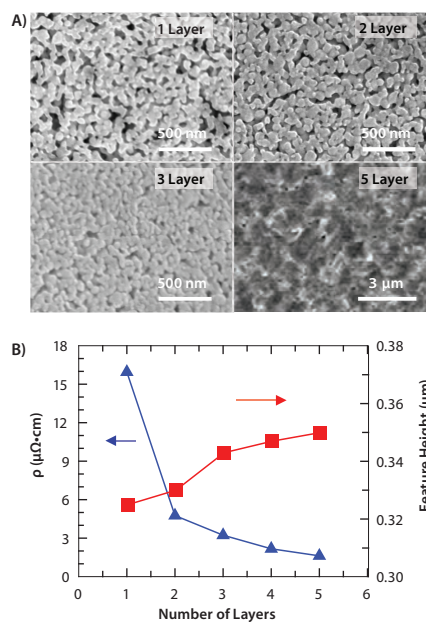


**Figure 3.** A) SEM micrographs of the silver microstructure as a function of layers. B) Electrical resistivity (triangle) and feature height (square) as a function of the number of layers deposited.

Because the single-layer silver electrodes are fairly conductive, we printed single-layer grid patterns (25 mm  $\times$  25 mm, line width = 80  $\mu\text{m}$ ) with a line spacing of 0.5 mm onto a poly(ethyleneterephthalate) (PET) substrate (**Figures 4A** and **B**). **Figure 4A** shows a high degree of transparency of the conductive single-layer grid; the text underneath is clearly visible through the printed grid. **Figure 4C** shows the transmittance of grid patterns deposited of varying line spacing of 0.5, 1.0, and 2.0 mm, respectively. At a grid spacing of 2 mm, a transmittance of above 90% was achieved.<sup>12</sup> The patterns were produced with a single drop-width, both horizontally and vertically, showing the ability of this modified reactive silver ink to be reliably jetted as well as wet and maintain high-fidelity patterned features on low-cost plastic substrates.

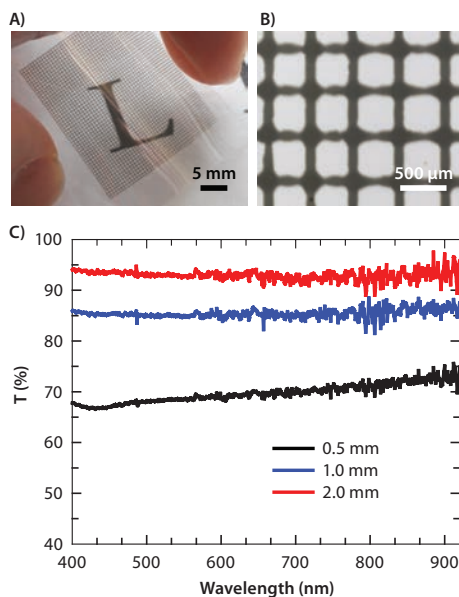


**Figure 4.** A) Optical and B) SEM images of transparent conductive square (25 mm × 25 mm) grid with 0.5 mm spacing between 80 μm features inkjet-printed on PET film. C) UV-Vis transmittance of conductive grids as a function of grid spacing.

## Summary

We have shown that by modifying reactive silver ink with the appropriate alkylamine ligand(s), we can vastly improve its ability to be patterned by inkjet printing without compromising the electrical performance at modest annealing temperatures (<120 °C). Because its viscosity and surface tension can be tailored over a broad range to facilitate multiple patterning approaches, this modified reactive silver ink opens new opportunities for printed electronics.

## Silver Inks

For a complete list of available conductive inks, visit [aldrich.com/inks](http://aldrich.com/inks).

Name	Silver Content	Viscosity	Form	Prod. No.
Reactive silver ink	12-14 wt. %	10-12 cP	liquid	<a href="#">745707-25ML</a>
Conductive silver printing ink, resistivity 30 - 35 μΩ-cm	65-75%	6000-9000 mPas	paste	<a href="#">791903-10G</a> <a href="#">791903-20G</a>
Conductive silver printing ink, resistivity 5-6 μΩ cm	75-85%	3000 mPas	paste	<a href="#">791873-10G</a> <a href="#">791873-20G</a>
Conductive silver printing ink, resistivity 9 - 10 μΩ-cm	75-85%	9000-12000 mPas	paste	<a href="#">791881-10G</a> <a href="#">791881-20G</a>

## Acknowledgment

This work was supported Office of Naval Research for financial support through the Multi-University Research Initiative (MURI Award N00014-11-1-0690). We gratefully acknowledge the use of facilities at the Frederick Seitz MRL Center for Microanalysis of Materials at the University of Illinois at Urbana-Champaign.

## References

- (1) (a) Galagan, Y., Andriessen, R., Rubingh, E., Grossiord, N., Blom, P., Veenstra, S., Verhees, W. and Kroon, J. *LOPE-C*, **2010**, 88; (b) Kaydanova, T., van Hest, M.F.A.M., Miedaner, A., Curtis, C.J., Alleman, J.L., Dabney, M.S., Garnett, E., Shaheen, S., Smith, L., Collins, R., Hanoka, J.L., Gabor, A.M. and Ginley, D. *NREL*, **2005**, 1; (c) Horteis, M., Grote, D., Binder, S., Filipovic, A., Schmidt, D. and Glunz, S.W. *IEEE*, **2009**, 000060.
- (2) (a) Feng, H., Cheng, R., Zhao, X., Duan, X. and Li, J. *Nat. Commun.*, **4**, 1539, 1; (b) Wu, H., Hu, L., Rowell, M.W., Kong, D., Cha, J.J., McDonough, J.R., Zhu, J., Yang, Y., McGehee, M.D. and Cui, Y. *Nano Lett.*, **2010**, *10*, 4242; (c) Doggart, J., Wu, Y., Liu, P. and Zhu, S. *ACS Appl. Mater. Interfaces*, **2010**, *2*, 2189.
- (3) (a) Wang, C.-T., Huang, K.-Y., Lin, D.T.W., Liao, W.-C., Lin, H.-W. and Hu, Y.-C. *Sensors*, **2010**, *10*, 5054; (b) Liu, X., Mwangi, M., Li, X., O'Brien, M. and Whitesides, G.M. *Lab Chip*, **2011**, *11*, 2189.
- (4) (a) Singh, S.K., Singh, M.K., Kulkarni, P.P., Sonkar, V.K., Grácio, J.J.A. and Dash, D. *ACS Nano*, **2012**, *6*, 2731; (b) Tian, B., Liu, J., Dvir, T., Jin, L., Tsui, J.H., Qing, Q., Suo, Z., Langer, R., Kohane, D.S. and Lieber, C.M. *Nat. Mater.*, **2012**, *11*, 986; (c) Kim, D.-H., Wang, S., Keum, H., Ghaffari, R., Kim, Y.-S., Tao, H., Panilaitis, B., Li, M., Kang, Z., Omenetto, F., Huang, Y. and Rogers, J.A. *Small*, **2012**, 2770.
- (5) (a) Lee, S.-H., Shin, K.-Y., Hwang, J.Y., Kang, K.T. and Kang, H.S. *J. Micromech. Microeng.*, **2008**, *18*, 075014; (b) Meier, H., Löffelmann, U., Mager, D., Smith, P.J. and Korvink J.G., *Phys. Status Solidi A*, **2009**, *206*, 1626; (c) Shankar, R., Groven, L., Amert, A., Whites, K.W. and Kellar, J.J. *J. Mater. Chem.*, **2011**, *21*, 10871.
- (6) (a) Ahn, B.Y., Duoss, E.B., Motala, M.J., Guo, X., Park, S.-I., Xiong, Y., Yoon, J., Nuzzo, R.G., Rogers, J.A. and Lewis, J.A. *Science*, **2009**, *323*, 1590; (b) Richards, V.N., Rath, N.P. and Buhro, W.E. *Chem. Mater.*, **2010**, *22*, 3556; (c) Wang, H., Qiao, X., Chen, J., Wang, X. and Ding, S. *Mater. Chem. Phys.*, **2005**, *94*, 449.
- (7) Perelaer, J., Smith, P.J., Mager, D., Soltman, D., Volkman, S.K., Subramanian, V., Korvink, J.G. and Schubert, U.S. *J. Mater. Chem.*, **2010**, *20*, 8446.
- (8) (a) Wu, Y., Li, Y. and Ong, B.S. *J. Am. Chem. Soc.*, **2006**, *128*, 4202; (b) Lee, J.J., Park, J.C., Kim, M.H., Chang, T.S., Kim, S.T., Koo, S.M., You, Y.C. and Lee, S.J. *J. Ceram. Processing Res.*, **2007**, *8*, 219; (c) Jahn, S.F., Jakob, A., Blaudeck, T., Schmidt, P., Lang, H. and Baumann, R.R. *Thin Solid Films*, **2010**, *518*, 3218; (d) Yasin, T. and Baktur, R. Antennas and Propagation Society International Symposium (APSURSI), 2010 *IEEE*, **2010**, 1; (e) Y. Wu, Y. Li and B. Ong, *J. Am. Chem. Soc.*, **2007**, *129*, 1862.
- (9) Chen, S.-P., Kao, Z.-K., Lin, J.-L. and Liao, Y.-C. *ACS Appl. Mater. Interfaces*, **2012**, 121207111315002
- (10) Walker, S.B. and Lewis, J.A. *J. Am. Chem. Soc.*, **2012**, *134*, 1419.
- (11) Derby, B. *Annu. Rev. Mater. Res.*, **2010**, *40*, 395.
- (12) (a) Layani, M., Gruchko, M., Milo, O., Balberg, I., Azulay, D. and Magdassi, S. *ACS Nano*, **2009**, *3*, 3537; (b) Ahn, B.Y., Lorang, D.J. and Lewis, J.A. *Nanoscale*, **2011**, *3*, 2700.

## Silver Nanoparticle Dispersions

For a complete list of available materials, visit [aldrich.com/nanosilver](http://aldrich.com/nanosilver).

Particle Size	Concentration	Applications	Prod. No.
particle size $\leq 10$ nm	50-60 wt. % in tetradecane	printing on ITO and glass	736511-25G 736511-100G
particle size $\leq 10$ nm	50-60 wt. % in tetradecane	printing on polyimide films	736503-25G 736503-100G
particle size $\leq 50$ nm	30-35 wt. % in triethylene glycol monoethyl ether	printing on ITO and glass	736481-25G 736481-100G
particle size $\leq 50$ nm	30-35 wt. % in triethylene glycol monomethyl ether	printing on ITO films	736473-25G 736473-100G
particle size $\leq 50$ nm	30-35 wt. % in triethylene glycol monomethyl ether	printing on plastic films	736465-25G 736465-100G

## Silver Nanowires

For a complete list of available materials, visit [aldrich.com/nanowires](http://aldrich.com/nanowires).

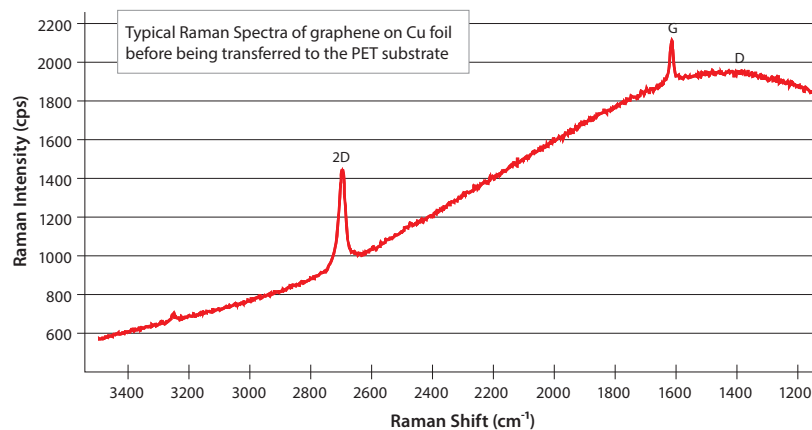
Diam. $\times$ L	Concentration	Form	Prod. No.
60 nm $\times$ 10 $\mu$ m	0.5% in isopropanol	liquid (suspension)	739421-25ML
115 nm $\times$ 20-50 $\mu$ m	0.5% in isopropanol	liquid (suspension)	739448-25ML
120-150 nm $\times$ 20-50 $\mu$ m	0.5% in isopropanol	liquid (suspension)	778095-25ML

### PRODUCT HIGHLIGHT

## Single-layer Graphene on PET

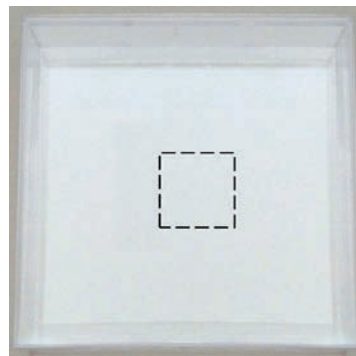
Providing the Ultimate Properties of Pristine Graphene

- 1 $\times$ 1-in. single-layer graphene on PET (Aldrich Prod. No. 745863)
- 2 $\times$ 2-in. single-layer graphene on PET (Aldrich Prod. No. 745871)
- Uniform Film Coverage with Excellent Thickness Consistency
- Highly Transparent and Conductive (>95% Transmittance;  $\sim$ 500  $\Omega$ /sq.)



### PET Film

Thickness	0.188 mm (0.0074 in.)
Haze	0.90%
Light Transmission	92%
Tensile Strength	MD: 179 MPa TD: 197 MPa
Tensile Elongation	MD: 132% TD: 99%
Coefficient of Static Friction	0.46
Coefficient of Kinetic Friction	0.4
Coefficient of Thermal Expansion	MD: 0.9% TD: 0.7%



Single-layer graphene on PET film

To explore our graphene products, visit  
[aldrich.com/graphene](http://aldrich.com/graphene)

# GRAPHENE-BASED TRANSPARENT CONDUCTIVE ELECTRODES

Kehan Yu<sup>1</sup> and Junhong Chen<sup>2\*</sup><sup>1</sup>Department of Chemical Engineering  
Case Western Reserve University Cleveland, Ohio 44106<sup>2</sup>Department of Mechanical Engineering

University of Wisconsin-Milwaukee, Milwaukee, Wisconsin 53211

\*jhchen@uwm.edu

## Introduction

A transparent conductive electrode (TCE) is an essential component of various optoelectronic devices such as solar cells, liquid-crystal displays (LCD), light-emitting diodes (LED), and touch screens.<sup>1-3</sup> The most commonly used TCEs are doped metal oxide-coated glasses, e.g., tin-doped indium oxide (ITO) (refer to the ITO-coated substrates on page 13), fluorine-doped tin oxide (FTO) (refer to the FTO-coated substrates table on page 13), and aluminum zinc oxide (AZO). However, metal oxide materials have several shortcomings that limit their usage by current industry and for future electronics. One major issue is the scarcity of the indium supply and the resulting increasing costs. In addition, ITO, together with its substitutes FTO and AZO, is brittle and thus unsuitable for applications in flexible and stretchable electronic devices.<sup>3,4</sup>

Emerging materials for fabricating TCEs include carbon nanotubes (CNTs), nanostructured metals (e.g., metal grids and metallic nanowires), and graphene (Figures 1A–C). It is generally accepted that substitute TCEs must have a sheet resistance of  $R_s < 100 \Omega/\text{sq.}$  coupled with transmittance  $T > 90\%$  in the visible range.<sup>5,6</sup> Large-area display and large-area solid-state lighting are even more demanding, with requirements of a sheet resistance below  $5 \Omega/\text{sq.}$ <sup>7</sup> A CNT network is severely limited by the large contact resistance of tube–tube junctions and, therefore, is still far from practical applications. A random network of Ag nanowires (AgNWs, Aldrich Prod. Nos. 778095, 739421 and 739448) can lead to an optoelectronic performance of  $10\text{--}20 \Omega/\text{sq.}$  with 90% optical transparency.<sup>8,9</sup>

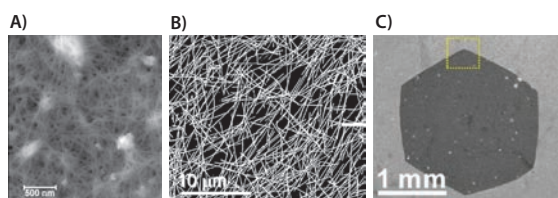


**Figure 1.** A) AFM image of a CNT network (reproduced with permission from Ref. 10, copyright 2007 American Chemical Society). B) SEM image of an AgNW network (reproduced with permission from Ref. 9, copyright 2009 American Chemical Society). C) SEM image of a graphene flake (reproduced with permission from Ref. 11, copyright 2012 American Chemical Society).

Graphene is a single layer of  $sp^2$  carbon atoms bonded in a honeycomb lattice. Graphene has remarkable properties:

- Intrinsic electron mobility ( $2 \times 10^5 \text{ cm}^2/\text{V}\cdot\text{s}$ ) enables high electrical conductivity<sup>12</sup>
- High thermal conductivity ( $\sim 5 \times 10^3 \text{ W/m}\cdot\text{K}$ ) can dissipate heat generated in power electronics<sup>13</sup>
- High mechanical strength can meet the need of flexible electronics
- Chemical stability makes graphene useful in harsh environments.

Graphene is transparent starting from the entire visible region through the far infrared. The minimum sheet resistance of an ideal undoped single-layer graphene (SLG) is about  $31 \Omega/\text{sq.}$  (free-standing single-layer graphene with room temperature mobility of  $2 \times 10^5 \text{ cm}^2/\text{V}\cdot\text{s}$  and carrier concentration of  $10^{12} \text{ cm}^{-2}$ ), which makes graphene a promising material for TCE applications. A  $p$ -doped monolayer graphene (Aldrich Prod. No. 773719) shows  $600 \Omega/\text{sq.}$  for  $T > 97\%$ . Coleman *et al.* predicted an upper limit  $R_s$  of undoped graphite film, e.g., few-layer graphene (FLG) at  $337 \Omega/\text{sq.}$  for  $T = 90\%$ .<sup>5</sup> This is far below the minimum requirement for industrial use since the intrinsic carrier concentration in graphene is low. However, for highly doped graphene  $R_s$  can be reduced to  $62.4/N \Omega/\text{sq.}$ , where  $N$  is the number of graphene layers in the film.<sup>14</sup> The theoretical transmittance of a free-standing graphene can be derived using Fresnel equations, giving  $T = 100 - 2.3N$  (%) depending on the number of layers  $N$ .<sup>15</sup> The absorbance per layer of graphene can be calculated as  $A = 1 - T = 2.3\%$ .<sup>15</sup> Therefore, four-layer graphene will result in an  $R_s$  of  $15 \Omega/\text{sq.}$  and  $T \sim 90\%$ , sufficient for most transparent conductor applications.

This article presents a brief summary of recent research on graphene-based TCEs. We discuss the use of graphene made using wet chemical methods and in gas phase and compare the advantages and disadvantages of each technique. The combination of graphene with other nanomaterials is also highlighted because of the excellent performance of the resulting TCEs. An outlook on the future development of graphene-based TCEs is also provided.

## Fundamentals

The crucial requirements for a TCE are high electrical conductivity and high optical transparency—very often a trade-off since electrical conductivity and optical transparency are oppositely controlled by the film thickness. Furthermore, the intrinsic properties of a material also limit the overall performance of a TCE. The transport in a solid-state conductor states that the DC conductivity  $\sigma_{\text{DC}}$  is proportional to the carrier concentration  $n$  (electron or hole), while optically, the classical Drude theory teaches that the plasma frequency (material's cutoff frequency in the optical transmittance spectrum) is proportional to the square root of  $n$ . This means that optical transmittance is sacrificed when improving the DC conductivity by increasing  $n$ . Explicitly, an ideal TCE is low in  $n$  and high in carrier mobility. On this basis, graphene is a unique TCE material that combines high electron mobility and low carrier concentration due to its outstanding two-dimensional electron gas. Assuming a lightly

doped graphene with free electron concentration ( $n \sim 10^{19} \text{ cm}^{-3}$  or  $10^{13} \text{ cm}^{-2}$ , eight or nine orders of magnitude lower than semiconductors or metals), the plasma wavelength is well shifted to far-infrared. However, with the high mobility of graphene ( $\sim 10^4 \text{ cm}^2/\text{V}\cdot\text{s}$  at room temperature), the DC conductivity is still considerably high.

Another issue for optimizing TCE performance is that the ( $R_s$ ,  $T$ ) pair cannot be compared directly for different TCEs. Aside from the carrier concentration  $n$  and carrier mobility  $\mu$ , the ( $R_s$ ,  $T$ ) of TCEs are primarily affected by the film thickness  $t$ . Therefore, an intrinsic measurement is needed for direct and accurate comparison of different materials at various thicknesses. For easy comparison, a recent study suggests a figure-of-merit (FOM).<sup>5</sup> Note that the sheet resistance of a conducting film is physically linked with its transparency. The sheet resistance is determined by DC conductivity  $\sigma_{\text{DC}}$ .

$$R_s = \frac{1}{\sigma_{\text{DC}} t} \quad (1)$$

The transmittance is controlled by optical conductivity  $\sigma_{\text{op}}$  by

$$T = \left(1 + \frac{Z_0}{2} \sigma_{\text{op}} t\right)^{-2} \quad (2)$$

where  $Z_0 = 377 \Omega$  is the impedance of free space. A combination of Equations 1 and 2 can eliminate the film thickness  $t$  and gives

$$T = \left(1 + \frac{Z_0}{2R_s} \frac{\sigma_{\text{op}}}{\sigma_{\text{DC}}}\right)^{-2} \quad (3)$$

The ( $R_s$ ,  $T$ ) pair is, therefore, only determined by the conductivity ratio (Equation 4). A high FOM will result in the desired TCE with a high  $T$  at a low  $R_s$

$$\text{FOM} = \frac{\sigma_{\text{DC}}}{\sigma_{\text{op}}} \quad (4)$$

The minimum industrial requirement ( $100 \Omega/\text{sq.}$ ,  $T=90\%$ ) can now be translated into  $\text{FOM} > 35$  using Equation 4. ITO has an FOM generally falling into the range 35–260 (Aldrich Prod. Nos. 703192 and 703184:  $8\text{--}60 \Omega/\text{sq.}$ ,  $T=84\%$ ).<sup>16</sup> As mentioned before, well-doped graphene can possess  $R_s = 62.4/N \Omega/\text{sq.}$  for  $T=100\text{--}2.3N$  (%) varying with the number of layers  $N$ ,<sup>14,15</sup> which results in FOMs ranging from 244 (4-layer) to 258 (single-layer). Although the FOM is a semi-empirical approach ( $T$  at 550 nm and neglecting the substrate contribution), it offers sufficiently high accuracy and facilitates the comparison among various TCEs.

We also compared graphene-based TCEs from the literature with those industry standards on the basis of FOM. In order to calculate FOMs of TCEs in the literature, sheet resistance and optical transmittance are extracted and fitted using Equation 3. Data from the literature, together with the calculated FOM, are plotted in Figure 2 and summarized in Table 1.

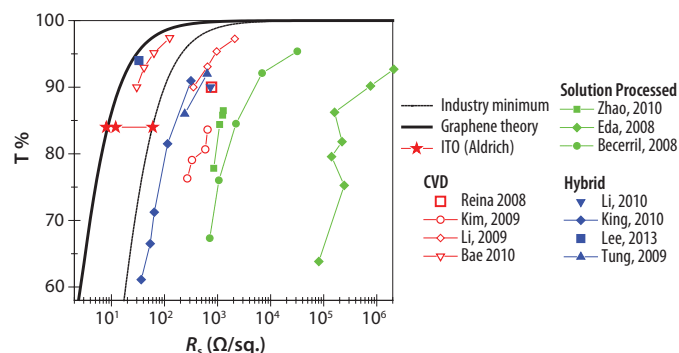


**Figure 2.** Transmittance and sheet resistance data reported in the literature. These are graphene films prepared by CVD (open red), solution processed graphene (solid green), and hybrid graphene film (solid blue). The red stars represent commercially available ITO. The dashed line illustrates the minimum industry standard for TCE (FOM=35). The solid line corresponds to the calculated case of highly doped graphene (FOM=244).

**Table 1.** Transmittance, sheet resistance, and FOM of graphene-based TCEs and commercially available ITO.

Material	T %	$R_s$ $\Omega/\text{sq.}$	FOM	Ref./Relevant Aldrich Product
ITO	84	8	259	703192
ITO	84	12	172	703192
ITO	84	60	34	703184
<b>Solution-processed</b>				
rGO	78	840	1.8	17
rGO	86	1.60E+05	8.70E-03	18
rGO	85	2200	1.2	19
<b>CVD</b>				
Grown with Ni	90	770	4.5	20
Grown with Ni	79	330	4.1	21
Grown with Cu	90	350	10	22
Grown with Cu	90	30	118	23
Grown with Cu	<97	600	27	773719
<b>Hybrid</b>				
CNT + rGO	86	240	10	24
CNT + CVD graphene	90	735	4.7	25
CNT + graphene	91	315	17.7	26
AgNW + graphene	94	33	182	27

## Solution-processed Graphene TCE

The solution process is likely the most suitable way to make large-scale TCE at the lowest cost. This technique is similar to that used for fabricating CNT TCEs. Typically, the solution process is divided into two steps: 1) breaking the graphite down to graphene flakes, and 2) fabricating the graphene thin film on substrates. Chemical exfoliation and ultrasonic exfoliation are mature techniques for the first top-down step in the solution phase. After purification (centrifugation), either the chemically converted graphene oxide (GO, Aldrich Prod. Nos. 763705 and 777676) or the sonically cleaved graphene flakes can form a stable suspension in the liquid phase, although the latter usually needs the assistance of a surfactant. The subsequent bottom-up fabrication includes filtration-transfer,<sup>18</sup> the Langmuir-Blodgett film technique,<sup>28,29</sup> spin-coating,<sup>14,19,30</sup> a liquid-air interface self-assembly,<sup>17</sup> and rod coating.<sup>31</sup> Note that relatively large sheet resistances of solution-processed graphene sheets arise from numerous small-sized grains and grain boundaries. A random network of solution-processed graphene flakes usually exhibits  $\text{FOM} < 0.7$  (with respect to a few hundred nm in lateral size), according to Coleman's survey.<sup>5</sup> The small FOM is due to the inter-flake junctions that are analogous to those of nanotube networks.

Chemical exfoliation of GO is accomplished by oxidizing inexpensive graphite powders using strong oxidants, and separated flakes are obtained by subsequent gentle exfoliation. A stable and clear aqueous GO suspension is obtained by washing, filtering, centrifuging, and re-dispersing in water. The GO is surface-functionalized with a high coverage of oxygen-containing groups and is, therefore, insulating. After coating on substrates, the GO thin film needs to be further converted to reduced graphene oxide (rGO, Aldrich Prod. No. 777684) for electrical conduction (Figure 3A). Technical details about oxidization and reduction were reviewed in a recent article.<sup>32</sup> GO flakes are usually small, most with an area on the order of  $100 \mu\text{m}^2$ , because of the unavoidable breaking of GO sheets during the vigorous oxidation.<sup>14,18,19,30,33-38</sup> Increasing rGO sheets to  $7,000 \mu\text{m}^2$ , Cheng et al. reported a TCE with  $840 \Omega/\text{sq.}$  at 78% transmittance (FOM=1.8, see Table 1).<sup>17</sup> Although many efforts have been devoted to developing a reduction technique, none can fully reduce GO and restore the exact graphene structure.<sup>32</sup> Without the removal of structural defects, the performance of solution-processed TCEs will hardly lead to further breakthroughs.

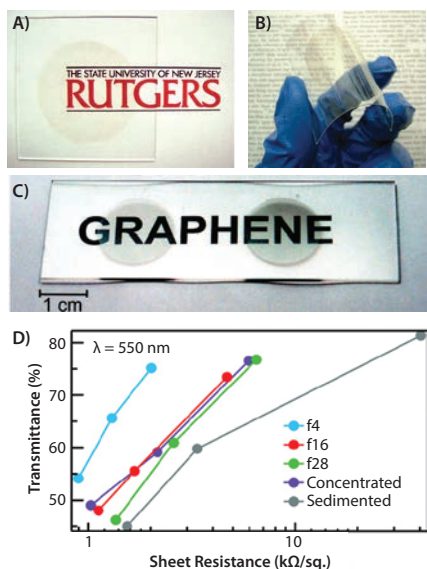


**Figure 3.** Thin films of solution-processed GO. Photographs of GO thin films on glass (A) and plastic (B) substrates (reproduced with permission from Ref. 18, copyright 2008 *Nature*). (C) Photograph of two sorted graphene transparent conductive films on glass. (D) Transmittance of graphene transparent conductors produced from different solutions as a function of their sheet resistance at a wavelength of 550 nm (reproduced with permission from Ref. 39, copyright 2009 American Chemical Society).

Avoiding oxidization and reduction, some direct liquid-phase methods were developed to produce pristine graphene. Coleman et al. pioneered the liquid-phase exfoliation of pristine graphene from bulk graphite with the organic solvents *N*-methylpyrrolidone (NMP, [Sigma-Aldrich Prod. No. 328634](#)), *N,N*-Dimethylacetamide (DMA, [Aldrich Prod. No. 185884](#)),  $\gamma$ -butyrolactone (GBL, [Aldrich Prod. No. B103608](#)), and 1,3-dimethyl-2-imidazolidinone (DMEU, [Aldrich Prod. No. 40725](#)), which are known to exfoliate CNTs.<sup>40</sup> Blake et al. simply exfoliated graphite by sonication in dimethylformamide (DMF, [Sigma-Aldrich Prod. No. 227056](#)) and obtained a well-dispersed suspension.<sup>41</sup> Green et al. prepared graphene by ultrasonication of graphite in water with the assistance of the planar surfactant sodium cholate.<sup>39</sup> With density gradient ultracentrifugation, they isolated graphene sheets with controlled thickness (**Figure 3A**). However, these techniques cannot yet bypass the limitation of grain boundaries (**Figure 3C**). TCEs with FOM>0.7 in this category are rarely reported.

## CVD Graphene TCE

Chemical vapor deposition (CVD) growth appears to be the most suitable approach to fabricate high-performance graphene film. Graphene growth with CVD on transition metal (mainly Ni and Cu) catalytic substrates results in a quality close to that of micro-mechanically exfoliated graphene from highly oriented pyrolytic graphite (HOPG); it readily forms a large-area thin film. Compared with the solution-processed graphene, the CVD graphene is primarily grown in a vacuum and can be costly. However, a reduced cost can be expected in scale-up production since low pressure CVD is compatible with the modern microelectronics industry.

Precursory research on graphene growth on a polycrystalline Ni film was reported by Kong's group and Hong's group.<sup>20,21</sup> The as-grown graphene film can be transferred to glass or plastic substrates by a poly[methyl methacrylate] (PMMA, [Aldrich Prod. Nos. 182230, 182265, 200336, and 445746](#))<sup>20</sup> or polydimethylsiloxane (PDMS, [Aldrich Prod. Nos. 423785, 482064 and 482145](#))<sup>21</sup> layer or just left on the PDMS surface as a flexible/stretchable film (**Figure 4A**). The resulting TCEs yield (770–1,000  $\Omega$ /sq.  $T=90\%$ )<sup>20</sup> and (280  $\Omega$ /sq.,  $T=76\%$ )<sup>21</sup>, which are equivalent to FOM=3.5–4.5

and 4.1, respectively. Alternatively, graphene TCE derived from CVD on Cu foil ([Aldrich Prod. No. 773697](#)) with a similar transfer technique has better performance than that from the Ni foil and can exhibit (350  $\Omega$ /sq.,  $T=90\%$ ), e.g., FOM~10.<sup>42</sup> The reason for the higher FOM with Cu is that the as-grown graphene is almost homogeneously single layer, while on Ni the graphene film has not only multiple layers but also variations in the number of layers.<sup>43</sup> Therefore, the charge carrier mobility is seriously affected by inhomogeneity (Refs. <sup>20</sup> vs. <sup>44</sup>).

A quick observation shows the FOM of CVD graphene is one order of magnitude higher than solution-processed graphene. This is also evidenced by Coleman's survey (FOM~10 for CVD graphene vs. ~0.7 for solution-processed graphene).<sup>5</sup> An immediate cause for the higher FOM is fewer structural defects in CVD graphene, which has been confirmed by micro-Raman spectroscopy numerous times in the literature. The Raman spectra of CVD graphene are almost identical with those of micro-mechanically exfoliated graphene from HOPG, whereas the solution-processed graphene (especially rGO) has an immortally high D peak indicating a large number of defects. A second contributing factor is the relatively large grain size for CVD graphene (several to tens of microns in lateral size) compared to the solution-processed ones (sub-micron in lateral size). Research shows a higher charge mobility with increasing graphene grain size,<sup>22</sup> and it can be as high as 10,400  $\text{cm}^2/\text{V}\cdot\text{s}$  for millimeter-size graphene.<sup>11</sup> TCEs fabricated with large-grain-size CVD graphene produce a considerably higher FOM when properly doped.

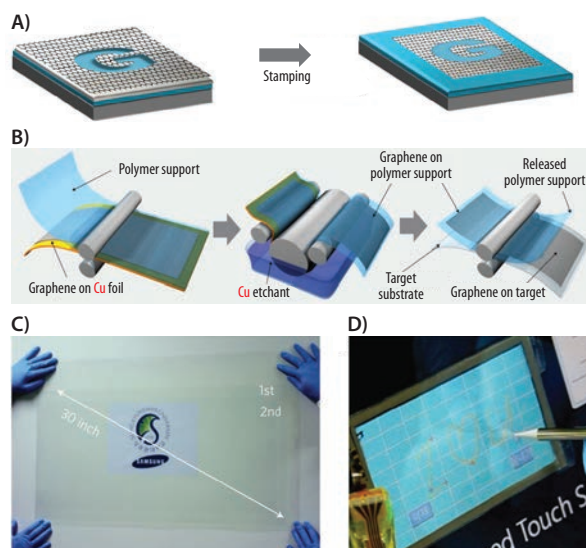


**Figure 4.** (A) Synthesis of patterned graphene films on thin nickel layers and transfer to substrate (reproduced with permission from Ref. 21, copyright 2009 *Nature*). (B) Schematic of the roll-based production of graphene films grown on a copper foil. (C) A transparent ultra large-area graphene film transferred on a 35-in. PET sheet. (D) A graphene-based touch-screen panel connected to a computer with control software. (B–D are reproduced with permission from Ref. 23, copyright 2010 *Nature*.)

A breakthrough toward real industrial-level TCE was demonstrated by large-area graphene growth on Cu foil and then transferring it to polyethylene terephthalate (PET) film using a roll-to-roll technique.<sup>23</sup> The results, displayed in **Figure 4**, show the roll-to-roll transfer of a graphene film grown on a flexible 30-in. PET substrate (**Figures 4B and C**). The authors demonstrated a large-area touch screen with the transferred graphene and claimed excellent optoelectronic performance over the entire substrate. With a four-layer graphene (repeatedly transferred, *p*-doped), the TCE exhibits (30  $\Omega$ /sq.  $T=90\%$ ) and a calculated FOM=118. These graphene-based TCEs already outperform ITO in some aspects and, therefore, make CVD graphene very promising for practical applications. More technical details about CVD growth of graphene and transfer are summarized by some excellent review articles and are beyond the scope of this paper.<sup>43,45,46</sup>

## Graphene-based Hybrid TCEs

One method to improve the conductivity of solution-processed graphene films is to incorporate a conductive filler material into them. Recently, some reports have emerged showing the benefits of incorporating CNTs into a matrix with graphene. Tung et al. mixed GO and CNT in anhydrous hydrazine (Sigma-Aldrich Prod. No. 215155) and spin-coated it on glass substrates (Figure 5A). After  $\text{SOCl}_2$  (thionyl chloride, Sigma-Aldrich Prod. No. 447285) doping, the TCE presents  $240 \Omega/\text{sq}$ ,  $T=86\%$ , equivalent to  $\text{FOM}=10$  (Figures 5B–C).<sup>24</sup> A hybrid of CNT and CVD graphene results in  $735 \Omega/\text{sq}$ ,  $T=90\%$ , which yields  $\text{FOM}\sim 4.7$ .<sup>25</sup> Using this hybrid film as a top electrode of an Si-based solar cell showed a power conversion efficiency of 5.2%.<sup>25</sup>

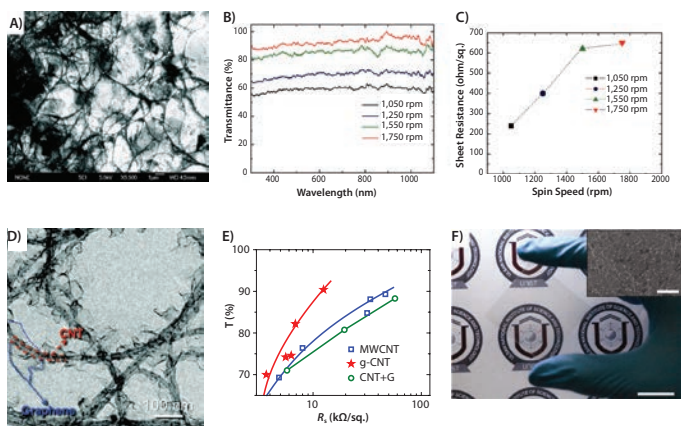


**Figure 5.** A) An SEM image of a solution-processed graphene-CNT hybrid film. B) Optical transmittance of the solution-processed graphene-CNT films as a function of different spin speeds. C) Sheet resistance versus different spin speeds (A–C reproduced with permission from Ref. 24, copyright 2009 American Chemical Society). D) TEM image of graphenated CNT (g-CNT) and E) its improvement on  $T$  versus  $R_s$  compared with a physical mixture of graphene and CNT (reproduced with permission from Ref. 47, copyright 2011 American Chemical Society). F) Photograph of graphene-AgNW hybrid film on a PET substrate. The scale bar indicates 2 cm. The inset shows an SEM image of this hybrid (scale bar, 5  $\mu\text{m}$ ) (reproduced with permission from Ref. 27, copyright 2013 American Chemical Society).

It is generally accepted that graphene and CNTs (or other filler material) mutually offer conduction pathways in a percolation network. However, the real role of mixing is still under debate since each component can introduce additional tube-flake junction resistance. One study argued the addition of graphene into a single-walled carbon nanotube (SWCNT) network cannot improve the FOM unless the hybrid is  $\text{SOCl}_2$ -treated.<sup>26</sup> More importantly, FOM changes non-monotonically with the film composition; the FOM peaks at 3% wt. graphene (40% higher than the nanotube-only film) and will decrease with more graphene content.<sup>26</sup> Yu et al. reported that covalently bonded CNT and graphene (known as graphenated CNT, i.e., g-CNT) can minimize the tube-flake junction resistance.<sup>48</sup> The graphene grown on the sidewall of a CNT with a plasma-enhanced chemical vapor deposition (PECVD) is inherently different from the physical mixture (Figure 5D).<sup>48</sup> The g-CNT can result in an FOM 44% higher than the CNT-only film and 64% higher than the physically mixed CNT-graphene film (Figure 5E).<sup>48</sup>

Another approach to high-performance TCEs is the hybrid of graphene and metallic nanowires. A recent report shows that an AgNW-graphene film (Figure 5F) exhibits an FOM as high as 182 ( $33 \Omega/\text{sq}$ ,  $T=94\%$  at 550 nm).<sup>27</sup> It is not surprising that the AgNW network has a high intrinsic conductivity; however, the graphene layer above or below the AgNWs introduces additional benefits. First, the graphene layer can dissipate heat and electrical stress and, thus, provides strong robustness against electrical breakdown. Second, the graphene layer covering AgNWs preserves TCE's electrical properties against thermal oxidation.

## Conclusion and Outlook

Will ITO eventually give way to graphene for TCEs? Although it is impossible to predict the future at this point, significant progress has been made in the past few years to improve the FOM of graphene-based TCEs from  $<1$  to  $>100$ . This has been accomplished by increasing the grain size and crystallinity, reducing defects, appropriate doping, and hybridizing with nanowires/nanotubes. Some recent progress in graphene research may spark further improvement in TCEs. For example, direct growth of graphene on dielectric substrates is one of the most interesting areas of research. Also, rapid progress made catalyst-free growth possible.<sup>47,49</sup> PECVD techniques enable low-temperature growth of graphene on  $\text{SiO}_2/\text{Si}$  (550–650  $^\circ\text{C}$ ), which can be compatible with the existing infrastructure of the microelectronics industry.<sup>50,51</sup> A recent study demonstrated direct growth of graphene on dielectric substrates at 400  $^\circ\text{C}$  by sophisticated control of a hydrocarbon+ $\text{H}_2$  plasma to balance etching and nucleation.<sup>52</sup> With this initial success, it is anticipated that direct growth of graphene on plastic substrates will become a reality—an ultimate goal of graphene TCE.

## Acknowledgments

Financial support for this work was provided by the U.S. Department of Energy (DE-EE0003208) and the U.S. National Science Foundation (ECCS-1001039).

## References

- Pang, S.; Hernandez, Y.; Feng, X.; Müllen, K. *Adv. Mater.* **2011**, *25*, 2779.
- He, M.; Jung, J.; Qiu, F.; Lin, Z. *J. Mater. Chem.* **2012**, *46*, 24254.
- Kumar, A.; Zhou, C. *ACS Nano* **2010**, *1*, 11.
- Sun, Y.; Rogers, J. A. *Adv. Mater.* **2007**, *15*, 1897.
- De, S.; Coleman, J.N. *ACS Nano* **2010**, *5*, 2713.
- [http://www.fep.fraunhofer.de/content/dam/fep/en/documents/Produktflyer/Advanced transparent conductive coatings on flat and flexible substrates\\_EN\\_V2.0\\_net.pdf](http://www.fep.fraunhofer.de/content/dam/fep/en/documents/Produktflyer/Advanced%20transparent%20conductive%20coatings%20on%20flat%20and%20flexible%20substrates_EN_V2.0_net.pdf)
- Eritt, M.; May, C.; Leo, K.; Toerker, M.; Radehaus, C. *Thin Solid Films* **2010**, *11*, 3042.
- Lee, J.-Y.; Connor, S.T.; Cui, Y.; Peumans, P. *Nano Lett.* **2008**, *2*, 689.
- De, S.; Higgins, T.M.; Lyons, P.E.; Doherty, E.M.; Nirmalraj, P.N.; Blau, W.J.; Boland, J.J.; Coleman, J.N. *ACS Nano* **2009**, *7*, 1767.
- Contreras, M.A.; Barnes, T.; van de Lagemaat, J.; Rumbles, G.; Coutts, T.J.; Weeks, C.; Glatkowski, P.; Levitsky, I.; Peltola, J.; Britz, D.A. *J. Phys. Chem. C* **2007**, *38*, 14045.
- Yan, Z.; Lin, J.; Peng, Z.; Sun, Z.; Zhu, Y.; Li, L.; Xiang, C.; Samuel, E.L.; Kittrell, C.; Tour, J.M. *ACS Nano* **2012**, *10*, 9110.
- Chen, J.-H.; Jang, C.; Xiao, S.; Ishigami, M.; Fuhrer, M.S. *Nature Nanotech.* **2008**, *4*, 206.
- Balandin, A.A.; Ghosh, S.; Bao, W.; Calizo, I.; Teweldebrhan, D.; Miao, F.; Lau, C.N. *Nano Lett.* **2008**, *3*, 902.
- Wu, J.; Agrawal, M.; Becerril, H.A.; Bao, Z.; Liu, Z.; Chen, Y.; Peumans, P. *ACS Nano* **2009**, *1*, 43.
- Nair, R.R.; Blake, P.; Grigorenko, A.N.; Novoselov, K.S.; Booth, T.J.; Stauber, T.; Peres, N.M.R.; Geim, A.K. *Science* **2008**, *5881*, 1308.
- Ellmer, K. *Nature Photon.* **2012**, *12*, 809.
- Zhao, J.; Pei, S.; Ren, W.; Gao, L.; Cheng, H.-M. *ACS Nano* **2010**, *9*, 5245.
- Eda, G.; Fanchini, G.; Chhowalla, M. *Nature Nanotech.* **2008**, *5*, 270.
- Becerril, H.A.; Mao, J.; Liu, Z.; Stoltenberg, R.M.; Bao, Z.; Chen, Y. *ACS Nano* **2008**, *3*, 463.
- Reina, A.; Jia, X.; Ho, J.; Nezich, D.; Son, H.; Bulovic, V.; Dresselhaus, M.S.; Kong, J. *Nano Lett.* **2008**, *1*, 30.
- Kim, K.S.; Zhao, Y.; Jang, H.; Lee, S.Y.; Kim, J.M.; Kim, K.S.; Ahn, J.-H.; Kim, P.; Choi, J.-Y.; Hong, B.H. *Nature* **2009**, *7230*, 706.
- Li, X.; Magnuson, C.W.; Venugopal, A.; An, J.; Suk, J.W.; Han, B.; Borysiak, M.; Cai, W.; Velamakanni, A.; Zhu, Y.; Fu, L.; Vogel, E.M.; Voelki, E.; Colombo, L.; Ruoff, R.S. *Nano Lett.* **2010**, *11*, 4328.
- Bae, S.; Kim, H.; Lee, Y.; Xu, X.; Park, J.-S.; Zheng, Y.; Balakrishnan, J.; Lei, T.; Ri Kim, H.; Song, Y.I.; Kim, Y.-J.; Kim, K.S.; Ozyilmaz, B.; Ahn, J.-H.; Hong, B.H.; Iijima, S. *Nature Nanotech.* **2010**, *8*, 574.
- Tung, V.C.; Chen, L.-M.; Allen, M.J.; Wassefi, J.K.; Nelson, K.; Kaner, R.B.; Yang, Y. *Nano Lett.* **2009**, *5*, 1949.
- Li, C.; Li, Z.; Zhu, H.; Wang, K.; Wei, J.; Li, X.; Sun, P.; Zhang, H.; Wu, D. *J. Phys. Chem. C* **2010**, *33*, 14008.
- King, P.J.; Khan, U.; Lotya, M.; De, S.; Coleman, J.N. *ACS Nano* **2010**, *7*, 4238.
- Lee, M.-S.; Lee, K.; Kim, S.-Y.; Lee, H.; Park, J.; Choi, K.-H.; Kim, H.-K.; Kim, D.-G.; Lee, D.-Y.; Nam, S.; Park, J.-U. *Nano Lett.* **2013**, *6*, 2814.
- Cote, L.J.; Kim, F.; Huang, J. *J. Am. Chem. Soc.* **2008**, *3*, 1043.
- Li, X.; Zhang, G.; Bai, X.; Sun, X.; Wang, X.; Wang, E.; Dai, H. *Nature Nanotech.* **2008**, *9*, 538.
- Wu, J.; Becerril, H.A.; Bao, Z.; Liu, Z.; Chen, Y.; Peumans, P. *Appl. Phys. Lett.* **2008**, *26*, 263302.
- Wang, J.; Liang, M.; Fang, Y.; Qiu, T.; Zhang, J.; Zhi, L. *Adv. Mater.* **2012**, *21*, 2874.
- Mao, S.; Pu, H.; Chen, J. *RSC Adv.* **2012**, *7*, 2643.

- (33) Mattevi, C., Eda, G., Agnoli, S., Miller, S., Mkhoyan, K.A., Celik, O., Mastrogianni, D., Granozzi, G., Garfunkel, E., Chhowalla, M. *Adv. Funct. Mater.* **2009**, *16*, 2577.
- (34) Liang, Y., Frisch, J., Zhi, L., Norouzi-Arasi, H., Feng, X., Rabe, J.P., Koch, N., Müllen, K. *Nanotechnol.* **2009**, *43*, 434007.
- (35) Wang, X., Zhi, L., Müllen, K. *Nano Lett.* **2007**, *1*, 323.
- (36) Zhao, L., Zhao, L., Xu, Y., Qiu, T., Zhi, L., Shi, G. *Electrochim. Acta* **2009**, *2*, 491.
- (37) Liu, Y., Gao, L., Sun, J., Wang, Y., Zhang, J. *Nanotechnol.* **2009**, *46*, 465605.
- (38) Eda, G., Lin, Y.-Y., Miller, S., Chen, C.-W., Su, W.-F., Chhowalla, M. *Appl. Phys. Lett.* **2008**, *23*.
- (39) Green, A.A., Hersam, M.C. *Nano Lett.* **2009**, *12*, 4031.
- (40) Hernandez, Y., Nicolosi, V., Lotya, M., Blighe, F.M., Sun, Z., De, S., McGovern, I.T., Holland, B., Byrne, M., Gun'ko, Y.K., Boland, J.J., Niraj, P., Duesberg, G., Krishnamurthy, S., Goodhue, R., Hutchison, J., Scardaci, V., Ferrari, A.C., Coleman, J.N. *Nature Nanotech.* **2008**, *9*, 563.
- (41) Blake, P., Brimicombe, P.D., Nair, R.R., Booth, T.J., Jiang, D., Schedin, F., Ponomarenko, L.A., Morozov, S.V., Gleason, H.F., Hill, E.W., Geim, A.K., Novoselov, K.S. *Nano Lett.* **2008**, *6*, 1704.
- (42) Li, X., Zhu, Y., Cai, W., Borysiak, M., Han, B., Chen, D., Piner, R.D., Colombo, L., Ruoff, R.S. *Nano Lett.* **2009**, *12*, 4359.
- (43) Mattevi, C., Kim, H., Chhowalla, M. *J. Mater. Chem.* **2011**, *10*, 3324.
- (44) Li, X., Cai, W., An, J., Kim, S., Nah, J., Yang, D., Piner, R., Velamakanni, A., Jung, I., Tutuc, E., Banerjee, S.K., Colombo, L., Ruoff, R.S. *Science* **2009**, *5932*, 1312.
- (45) Zhang, Y., Zhang, L., Zhou, C. *Acc. Chem. Res.* **2013**, *10*, 2329.
- (46) Chen, Y.P., Yu, Q., Newell, D., Wu, W., Jauregui, L.A., Cao, H., Shen, T., Chung, T.F. *Int. J. Mod. Phys. B* **2013**, *10*, 1341002.
- (47) Chen, J., Wen, Y., Guo, Y., Wu, B., Huang, L., Xue, Y., Geng, D., Wang, D., Yu, G., Liu, Y. *J. Am. Chem. Soc.* **2011**, *44*, 17548.
- (48) Yu, K., Lu, G., Bo, Z., Mao, S., Chen, J. *J. Phys. Chem. Lett.* **2011**, *13*, 1556.
- (49) Hwang, J., Kim, M., Campbell, D., Alsalman, H.A., Kwak, J.Y., Shivaraman, S., Woll, A.R., Singh, A.K., Hennig, R.G., Gorantla, S., Rummeli, M.H., Spencer, M.G. *ACS Nano* **2012**, *1*, 385.
- (50) Zhang, L., Shi, Z., Wang, Y., Yang, R., Shi, D., Zhang, G. *Nano Res.* **2011**, *3*, 315.
- (51) Yang, W., He, C., Zhang, L., Wang, Y., Shi, Z., Cheng, M., Xie, G., Wang, D., Yang, R., Shi, D., Zhang, G. *Small* **2012**, *9*, 1429.
- (52) Wei, D., Lu, Y., Han, C., Niu, T., Chen, W., Wee, A.T.S. *Angew. Chem., Int. Ed.* **2013**, 14121.

## Graphene

For a complete list of available materials, visit [aldrich.com/graphene](http://aldrich.com/graphene).

Name	Sheet Resistance	Prod. No.
Monolayer graphene film, 1 cm x 1 cm on copper foil	600 Ω/sq	773697-4EA
Monolayer graphene film, 1 cm x 1 cm on quartz	600 Ω/sq	773719-4EA
Monolayer graphene film, 1 cm x 1 cm on SiO <sub>2</sub> /Si substrate	600 Ω/sq	773700-4EA
Monolayer graphene film, 1 in. x 1 in. on PET film	700 Ω/sq	745863-1EA 745863-5EA
Monolayer graphene film, 2 in. x 2 in. on PET film	700 Ω/sq	745871-1EA

## Graphene Oxide (GO)

For a complete list of available materials, visit [aldrich.com/graphene](http://aldrich.com/graphene).

Name	Concentration	Form	Prod. No.
Reduced graphene oxide	-	powder	777684-250MG 777684-500MG
Graphene oxide	2 mg/mL	dispersion in H <sub>2</sub> O	763705-25ML 763705-100ML
Graphene oxide	4 mg/mL	dispersion in H <sub>2</sub> O	777676-50ML 777676-200ML
Graphene oxide, ammonia functionalized	1 mg/mL	dispersion in H <sub>2</sub> O	791520-25ML 791520-100ML

## Carbon Nanotubes (CNTs)

### Single-walled Carbon Nanotube Ink

For a complete list of available materials, visit [aldrich.com/swnt](http://aldrich.com/swnt).

SWCNT Concentration	Viscosity	Sheet Resistance	Form	Prod. No.
0.20 +/- 0.01 g/L (by Absorbance at 854 nm)	viscosity ~1.0 mPa.s	resistance <400 Ω/sq (by 4-point probe on prepared film by spray)	dispersion in H <sub>2</sub> O	791490-25ML 791490-100ML
1.00 +/- 0.05 g/L (by Absorbance at 854 nm)	viscosity 3.0 mPa.s (at 10 sec <sup>-1</sup> shear rate)	resistance <600 Ω/sq (by 4-point probe on prepared film by spray)	dispersion in H <sub>2</sub> O	791504-25ML 791504-100ML

### Single-walled Carbon Nanotubes (SWCNTs)

For a complete list of available materials, visit [aldrich.com/swnt](http://aldrich.com/swnt).

Production Method	Dimensions	Purity	Prod. No.
CoMoCAT® Catalytic Chemical Vapor Deposition (CVD) method	diameter 0.6 - 1.1 nm	>95% (carbon as SWCNT)	775533-250MG 775533-1G
CoMoCAT® Catalytic Chemical Vapor Deposition (CVD) Method (6,5) chirality carbon >= 95%	diameter 0.7 - 0.9 nm (by fluorescence)	≥93% (carbon as SWNT)	773735-250MG 773735-1G
CoMoCAT® Catalytic Chemical Vapor Deposition (CVD) Method (7,6) chirality	diameter 0.7 - 1.1 nm L 300-2300 nm (mode: 800 nm; AFM)	≥77% (carbon as SWNT)	704121-250MG 704121-1G
CoMoCAT® Catalytic Chemical Vapor Deposition (CVD) Method (6,5) chirality	diameter 0.7 - 0.9 nm (by fluorescence) L ≥700 nm	≥77% (carbon as SWNT)	704148-250MG 704148-1G
CoMoCAT® Catalytic Chemical Vapor Deposition (CVD) Method	diameter 0.7 - 1.4 nm	≥80.0% (carbon as SWNT)	724777-250MG 724777-1G
CoMoCAT® Catalytic Chemical Vapor Deposition (CVD) Method	diameter 0.7 - 1.3 nm L 450-2300 nm (mode: 800 nm; AFM)	≥70% (carbon as SWNT)	704113-250MG 704113-1G

Production Method	Dimensions	Purity	Prod. No.
Catalytic Carbon Vapor Deposition (CCVD) Method	average diameter 2 nm L x 3 (TEM)	>70%, TGA	755710-250MG 755710-1G
Electric Arc Discharge Method	diameter 1.2 - 1.7 nm L 0.3-5 $\mu$ m	30% (Metallic) 70% (Semiconducting)	750492-100MG
Electric Arc Discharge Method	diameter 1.2 - 1.7 nm L 0.3-5 $\mu$ m	70% (Semiconducting) 30% (Metallic)	750514-25MG
Electric Arc Discharge Method	diameter 1.2 - 1.7 nm L 0.3-5 $\mu$ m	2% (Metallic) 98% (Semiconducting)	750522-1MG
Electric Arc Discharge Method	diameter 1.2 - 1.7 nm L 0.3-5 $\mu$ m	2% (Semiconducting) 98% (Metallic)	750530-1MG
Electric Arc Discharge Method	D x L 2-10 nm x 1-5 $\mu$ m (bundle dimensions) 1.3-1.5 nm (individual SWNT diameter)	40-60 wt. % carbon basis	698695-1G 698695-5G

## Double-walled Carbon Nanotubes (DWCNTs)

For a complete list of available materials, visit [aldrich.com/dwnt](http://aldrich.com/dwnt).

Production Method	Dimensions	Purity	Prod. No.
Catalytic Carbon Vapor Deposition (CCVD) Method	avg. diam. x L 3.5 nm x >3 $\mu$ m (TEM)	Metal Oxide $\leq$ 10% TGA	755141-1G
Catalytic Carbon Vapor Deposition (CCVD) Method	avg. diam. x L 3.5 nm x 1-10 $\mu$ m (TEM)	Metal Oxide <10% TGA	755168-1G
Chemical Vapor Deposition (CVD) Method	O.D. x I.D. x L 5 nm x 1.3-2.0 nm x 50 $\mu$ m	50-80% carbon basis	637351-250MG 637351-1G

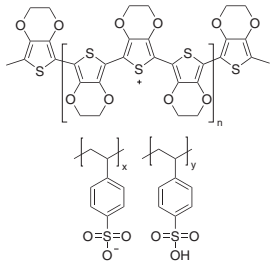
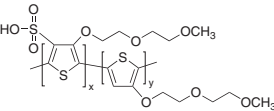
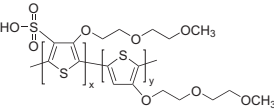
## Multi-walled Carbon Nanotubes (MWCNTs)

For a complete list of available materials, visit [aldrich.com/mwnt](http://aldrich.com/mwnt).

Production Method	Description	Purity	Prod. No.
CoMoCAT® Catalytic Chemical Vapor Deposition (CVD) Method	O.D. x I.D. x L 10 nm $\pm$ 1 nm x 4.5 nm $\pm$ 0.5 nm x 3~6 $\mu$ m (TEM)	$\geq$ 98% carbon basis	773840-25G 773840-100G
CoMoCAT® Catalytic Chemical Vapor Deposition (CVD) Method	O.D. x L 6-9 nm x 5 $\mu$ m diam. 5.5 nm (mode) diam. 6.6 nm (median)	>95% (carbon)	724769-25G 724769-100G
CoMoCat® Catalytic Chemical Vapor Deposition (CVD) Method	O.D. x I.D. x L 10 nm x 4.5 nm x 4 $\mu$ m	70-80%, TGA (Carbon content)	791431-25G 791431-100G
Catalytic Carbon Vapor Deposition (CCVD) Method	avg. diam. x L 9.5 nm x <1 $\mu$ m (TEM) thin and short	Metal Oxide <5% TGA	755117-1G
Catalytic Carbon Vapor Deposition (CCVD) Method	avg. diam. x L 9.5 nm x 1.5 $\mu$ m (TEM) thin	Metal Oxide <5% TGA	755133-5G
Chemical Vapor Deposition (CVD) Method	O.D. x L 6-13 nm x 2.5-20 $\mu$ m 10 $\mu$ m (average length, TEM) 12 nm (average diameter, HRTEM)	>98% carbon basis	698849-1G
Chemical Vapor Deposition (CVD) Method	D x L 110-170 nm x 5-9 $\mu$ m	>90% carbon basis	659258-2G 659258-10G
Electric Arc Discharge Method	O.D. x L 7-12 nm x 0.5-10 $\mu$ m powdered cylinder cores	20-30% MWCNT basis	406074-500MG 406074-1G 406074-5G
Electric Arc Discharge Method	O.D. x L 7-15 nm x 0.5-10 $\mu$ m as-produced cathode deposit	>7.5% MWCNT basis	412988-100MG 412988-2G 412988-10G
Plasma-Enhanced Chemical Vapor Deposition (PECVD) Method	diam. x L 100-150 nm x 30 $\mu$ m (SEM) vertically aligned on silicon wafer substrate	>95 atom % carbon basis (x-ray)	687804-1EA
Plasma-Enhanced Chemical Vapor Deposition (PECVD) Method	diam. x L 100 nm $\pm$ 10% x 30 $\mu$ m $\pm$ 10% vertically aligned on copper wafer substrate	>99.9% carbon basis	687812-1EA

## Organic Conductive Inks

For a complete list of available materials, visit [aldrich.com/inks](http://aldrich.com/inks).

Structure	Name	Concentration (%)	Viscosity (cP)	Other Properties	Prod. No.
	Poly(3,4-ethylenedioxythiophene)-poly(styrenesulfonate)	0.8 in H <sub>2</sub> O	7-12 at 22 °C	resistance 75-120 Ω/sq (>80% visible light transmission, 40 μm wet)	<a href="#">739316-25G</a>
	Poly(thiophene-3-[2-(2-methoxyethoxy)ethoxy]-2,5-diyl), sulfonated	2 in 1,2-propanediol/isopropanol/water, 3:2:1	7-13 (Brookfield)	resistivity 25-250 Ω-cm work function -5.1--5.2 eV	<a href="#">699799-25ML</a>
		2 in ethylene glycol monobutyl ether/water, 3:2	4.0-10.0 (Brookfield)	resistivity 500-3,000 Ω-cm work function -5.1--5.2 eV	<a href="#">699780-25ML</a>
	Plexcore® OC RG-1110 organic conductive ink	2.1	8.3 at 25 °C	resistivity 10-300 Ω-cm	<a href="#">719110-25ML</a>
	Plexcore® OC RG-1115 organic conductive ink	2.0	8.7 at 25 °C	resistivity 10-300 Ω-cm work function 4.8 eV	<a href="#">719129-25ML</a>
	Plexcore® OC RG-1150 organic conductive ink	2.0	8.0 at 25 °C	resistivity 300-1000 Ω-cm work function 4.8 eV	<a href="#">719137-25ML</a>
	Plexcore® OC RG-1155 organic conductive ink	2.0	8.6 at 25 °C	resistivity 300-1000 Ω-cm	<a href="#">719145-25ML</a>

## Ink Kits

For a complete list of available materials, visit [aldrich.com/inks](http://aldrich.com/inks).

Name	Application	Prod. No.
Organic conductive inks kit	Organic Conductive Inks for printed electronics applications including OLED devices.	<a href="#">719102-1KT</a>
Organic photovoltaic ink system	Ready-to-use organic ink system for bulk heterojunction solar cells and spin coating.	<a href="#">711349-1KT</a>
Organic photovoltaic ink system, PV 2000 kit	Ready-to-use organic ink system for bulk heterojunction solar cells and spin coating.	<a href="#">772364-1KT</a>

## Indium Tin Oxide (ITO) Coated Substrates

For a complete list of available materials, visit [aldrich.com/ito](http://aldrich.com/ito).

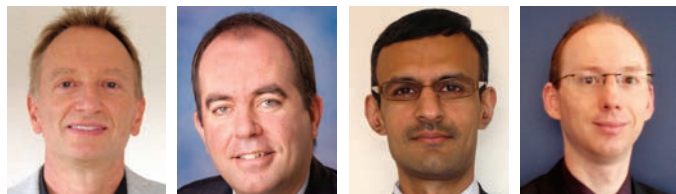
Description	L x W x Thickness (mm)	Surface Resistivity ( $\Omega/\text{sq}$ )	Prod. No.	
Indium tin oxide coated PET	1 ft x 1 ft x 5 mil	60	639303-1EA 639303-5EA	
	1 ft x 1 ft x 5 mil	100	639281-1EA 639281-5EA	
	1 ft x 1 ft x 5 mil	200	749745-1EA 749745-5EA	
	1 ft x 1 ft x 5 mil	250	749761-1EA 749761-5EA	
	1 ft x 1 ft x 5 mil	300	749796-1EA 749796-5EA	
	1 ft x 1 ft x 7 mil	60	749729-1EA 749729-5EA	
	1 ft x 1 ft x 7 mil	100	749737-1EA 749737-5EA	
	1 ft x 1 ft x 7 mil	200	749753-1EA 749753-5EA	
	1 ft x 1 ft x 7 mil	250	749788-1EA 749788-5EA	
	1 ft x 1 ft x 7 mil	300	749818-1EA 749818-5EA	
	Indium tin oxide coated glass slide, square	25 x 25 x 1.1	8-12	703192-10PAK
		25 x 25 x 1.1	30-60	703184-10PAK
25 x 25 x 1.1		70-100	703176-10PAK	
Indium tin oxide coated glass slide, rectangular	75 x 25 x 1.1	8-12	578274-10PAK 578274-25PAK	
	75 x 25 x 1.1	15-25	636916-10PAK 636916-25PAK	
	75 x 25 x 1.1	30-60	636908-10PAK 636908-25PAK	
	75 x 25 x 1.1	70-100	576352-10PAK 576352-25PAK	
Indium tin oxide coated boro-aluminosilicate glass slide	75 x 25 x 1.1	5-15	576360-10PAK 576360-25PAK	

## Fluorine-doped Tin Oxide (FTO) Coated Substrates

For a complete list of available materials, visit [aldrich.com/fto](http://aldrich.com/fto).

Description	L x W x D (mm)	Surface Resistivity ( $\Omega/\text{sq}$ )	Prod. No.
Fluorine doped tin oxide coated glass slide	50 x 50 x 2.2	~7	735140-5EA
	50 x 50 x 3	~8	735175-5EA
	50 x 50 x 3	~10	735205-5EA
	50 x 50 x 2.2	~13	735248-5EA
	100 x 100 x 2.3	~7	735159-5EA
	100 x 100 x 3	~8	735183-5EA
	100 x 100 x 3	~10	735213-5EA
	100 x 100 x 2	~13	735256-5EA
	300 x 300 x 2	~7	735167-1EA
	300 x 300 x 3.2	~8	735191-1EA
	300 x 300 x 3	~10	735221-1EA
	300 x 300 x 2.3	~13	735264-1EA

# UNDERSTANDING AND SUCCESSFULLY APPLYING MATERIALS FOR DYE-SENSITIZED SOLAR CELLS



Hans Desilvestro, Yanek Hebting, Mikael Khan, Damion Milliken  
Dyesol, Queanbeyan NSW 2620, Australia  
Email: yhebting@dyesol.com

## Introduction

While dye sensitization as the basis for color photography has been accepted for a very long time,<sup>1</sup> attempts to use this principle for the conversion of solar light to electricity generally had resulted only in very low photocurrents, below 100 nA/cm<sup>2</sup>.<sup>2</sup> In the mid-1980s, chemisorption of ruthenium-based dyes on high surface area titanium dioxide (titania or TiO<sub>2</sub>) through carboxylate bonds resulted in unprecedented photocurrents in the mA/cm<sup>2</sup> range and incident photon-to-current conversion efficiency [IPCE, also called external quantum efficiency (EQE)] of up to 44%.<sup>3</sup> Shortly thereafter, the dye-sensitized solar cell (DSC) was invented based on mesoporous TiO<sub>2</sub> and an organic electrolyte system containing the I<sub>3</sub><sup>-</sup>/I<sup>-</sup> redox couple.<sup>4,5</sup> Since these pioneering days, DSC development has attracted much interest from academia and industry due to prospects of its greater performance, particularly under non-ideal and diffuse light conditions, paired with relatively low cost and low energy manufacturing processes, and the options of light weight, flexibility, and partial transparency.<sup>6</sup> While DSCs fabricated with traditional solvents and redox couples have reached efficiencies of 12.3%<sup>7</sup> under Air Mass (AM) 1.5-type illumination, more recently, titania-based solid-state devices have been reported with laboratory efficiencies of 15%.<sup>8,9</sup> This article describes the core materials required for successful assembly of DSC devices and their interaction in a photovoltaic device.

## Main Components of Dye-sensitized Solar Cells

In general, the main components of DSCs are TiO<sub>2</sub>, ruthenium-based dyes, liquid electrolytes, platinum electrocatalysts, and silver inks. Each component material shows many interrelationships between different materials. If one DSC component is changed, e.g., the dye, other components such as TiO<sub>2</sub> particle size, film thickness, or the electrolyte composition may need adjustment to ensure optimum system performance. **Figure 1** shows the key components of a DSC, arranged from top to bottom, in the direction of incident light:

- Transparent substrate
- Layer of Transparent Conductive Oxide (TCO)

- Layer of mesoporous TiO<sub>2</sub> having its surface covered by a monomolecular layer of dye
- Electrolyte solution filling the pores of the dyed TiO<sub>2</sub> film and a thin layer between TiO<sub>2</sub> and counter electrode
- Very thin coating of electrocatalyst, such as Pt
- Counter electrode substrate coated with a thin layer of TCO
- Perimeter seal and possibly fill hole seal if long-term stability is required
- Two current collector bus bars to maximize current collection efficiency (optional)

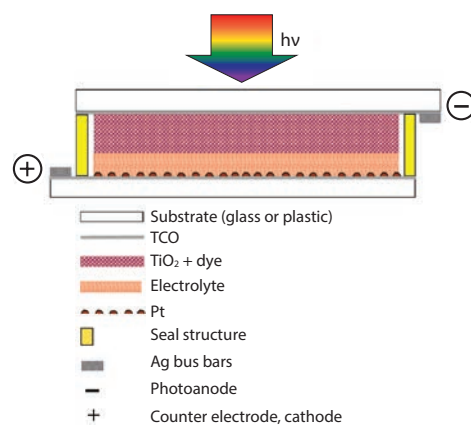


**Figure 1.** Schematic of the architecture and main components of a dye-sensitized solar cell.

## TiO<sub>2</sub> Pastes and Films

Titania is a widely available, nontoxic material used in everyday products such as toothpaste, sunscreens and paints. DSC technology requires the most active titania (anatase polymorph), in contrast to the paint industry where TiO<sub>2</sub> has to be photochemically desensitized to minimize resin decomposition, yellowing, blistering, etc.<sup>10</sup> Anatase TiO<sub>2</sub> ([Aldrich Prod. No. 637254](#)) is an *n*-type semiconductor and has a band gap of 3.2 eV, which corresponds to an optical onset of around 390 nm for light absorption. In traditional photovoltaic panels, solar-grade silicon requires 99.9999% purity (i.e., less than 1 ppm total impurities).<sup>11</sup> In comparison, requirements for anatase TiO<sub>2</sub> in DSC are less stringent but nevertheless important, and high-quality titania feedstock such as those used for the preparation of 18NR pastes ([Aldrich Prod. Nos. 791547](#) and [791555](#)) have a phase purity of at least 99%. Other popular titania products for DSC research show a much lower phase purity, with considerable amounts of rutile as well as amorphous TiO<sub>2</sub>,<sup>12</sup> thereby limiting the performance of the system.

Performance in a DSC not only depends on TiO<sub>2</sub> chemical and phase purity, but on additional factors such as particle size and distribution, shape, surface hydroxylation, application methods, and sintering. Paste formulation, printing, drying and sintering parameters need to be carefully controlled to achieve the best optimized results. These parameters influence film morphology, overall porosity, and pore size distribution. 18NR-T (Transparent, Aldrich Prod. No. 791547) and AO (Active Opaque, Aldrich Prod. No. 791555) titania pastes have been used for record-breaking DSC work.<sup>8</sup> Under recommended screen printing and firing conditions, 18NR-T paste results in optically transparent 6–7 μm thick films and a film porosity of ca. 65%. Depending on the dye employed, 1 to 3 layers may be required. Alternatively, screens of larger or smaller mesh size can be employed to finely adjust overall film thickness.

Figure 2 shows an SEM image of a sintered 18NR-T film. The average particle size is ca. 20 nm. The nanoparticulate and mesoporous nature (i.e., pores with diameters between 2 and 50 nm) of titania electrodes in DSCs is important from at least five aspects:

- Optically to provide transparent films due to the particle size being significantly smaller than the wavelength of visible light.
- Electronically to avoid the formation of interfacial space charge layers, which would reduce device voltage. Since the particles are much smaller than the width of the space charge layer in a corresponding semiconductor (TiO<sub>2</sub>) based on much larger particles, no such layer is formed at the solid/electrolyte interface. Instead, electrons diffuse freely in the TiO<sub>2</sub> conduction band. Their charge is effectively screened by positive ions in the electrolyte, which facilitates their transport through the TiO<sub>2</sub> particle network.
- Mechanically and electronically to facilitate particle-to-particle connections at relatively low temperatures of ca. 500 °C. Larger grain titania particles can only be fused together at much higher temperatures, around 800 °C and above.
- High surface area for dye adsorption is required to ensure effective harvesting of the maximum possible incident light.
- Open porous structure, necessary for penetration of both dye molecules to anchor to titania and electrolyte ions to regenerate the dye once oxidized during device operation.

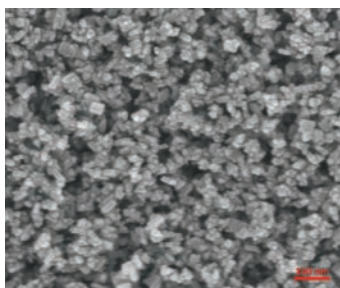


Figure 2. SEM of 18NR-T paste-based TiO<sub>2</sub> film after sintering.

While transparent films offer the potential of semi-transparency of the final products for windows or skylight applications, they often do not allow for sufficient absorption of longer wavelength light. Therefore, some light scattering and internal reflection are desirable. This can be achieved in two ways, either by adding larger light scattering TiO<sub>2</sub> particles to the titania paste or by adding a scattering layer on top of a transparent layer.

The former has advantages that the overall titania film thickness is not increased significantly; the added larger particles (up to 450 nm diameter in the case of 18NR-AO) not only contribute to performance through their light scattering effect, but actively through adsorption of dye and, hence, additionally enhance light conversion. Processing a single paste is also more convenient than a bi-layer structure. Addition of relatively large scattering particles leads to an increase of haze, which is defined according to Equation 1:

$$\text{Haze}(\lambda) = T_d(\lambda)/T_{\text{tot}}(\lambda) = (1 - T_s(\lambda))/T_{\text{tot}}(\lambda) \quad (1)$$

where  $T_d(\lambda)$  is the diffuse (or scattered) transmittance at wavelength  $\lambda$ ,  $T_s$  the specular transmittance, and  $T_{\text{tot}}$  the total transmittance. Haze of a 15 μm film based on 18NR-AO paste (Aldrich Prod. No. 791555) is significantly above 99% over the entire visible spectrum. Device performance increases with haze at longer wavelengths (e.g., at 800 nm).<sup>13</sup> 18NR-AO paste is particularly suitable whenever highest conversion efficiency is required, especially when higher viscosity electrolytes are used. It facilitates the use of thinner titania films, which is advantageous in reducing tortuosity and improving electrolyte mobility.<sup>14</sup> Employing 18NR-AO paste under the recommended screen printing and firing conditions results in white, opaque 7–8 μm thick films and a film porosity of ca. 55–60%. Similar to 18NR-T, 1 to 3 layers may be required depending on the nature of sensitizing dye, and screens of larger or smaller mesh size can be used to adjust overall film thickness.

When maximum output is sought, a scattering layer based on WER2-O reflector titania paste (Aldrich Prod. No. 791539) can significantly enhance IPCE, particularly at longer wavelengths where dye absorption becomes weaker. WER2-O contains well-dispersed, largely DSC-inactive scattering particles of 150–250 nm diameter. A 3 μm thick layer leads to a completely opaque white film on top of a transparent active film.

## Dyes

The dye can be considered the heart of DSCs. Its absorption spectrum and electronic coupling to *n*-type electron conductor determine absorption ( $\eta_{\text{abs}}$ ) and electron injection efficiency ( $\eta_{\text{inj}}$ ), which are two of the three key contributors to IPCE:

$$\text{IPCE}(\lambda) = \eta_{\text{abs}}(\lambda) \times \eta_{\text{inj}}(\lambda) \times \eta_{\text{coll}}(\lambda) \quad (2)$$

Considerable internal area is available for dye adsorption in titania films. The amount of dye adsorbed can be determined using chemical dye desorption and spectrophotometry methods.<sup>15</sup> Typically for N719 (Aldrich Prod. No. 703214), the amount of adsorbed dye is  $1.1 \times 10^7$  mol per cm<sup>2</sup> of projected area. Based on a film thickness ( $d_{\text{TiO}_2}$ ) of 14 μm, this corresponds to a dye concentration within the film,  $c_{\text{TiO}_2}^{\text{dye}} = 7.8 \times 10^{-5}$  mol per cm<sup>3</sup>. For a transparent film, the amount of absorbed light, i.e., the light not transmitted ( $=1-T$ ), can be estimated from Equation 3:

$$1-T = 1 - 10^{-\epsilon c_{\text{TiO}_2}^{\text{dye}} d_{\text{TiO}_2}} \quad (3)$$

If the extinction coefficient  $\epsilon$  is, through adsorption on TiO<sub>2</sub>, not altered significantly from its  $\epsilon_{\text{max}}$  of value in solution ( $14,700 \text{ M}^{-1}\text{cm}^{-1}$  for N719), such an amount of dye can absorb 97.5% of the light at the absorption maximum. Note, however, that the absorption spectrum is red-shifted upon adsorption on TiO<sub>2</sub>. Assuming a surface roughness factor of ca. 1,300, each N719 molecule occupies an area of ca. 2 nm<sup>2</sup>. This figure is higher by 30–70% compared to the theoretically estimated 'foot print' of N3<sup>16</sup> (Aldrich Prod. No. 703206), indicating that not all TiO<sub>2</sub> sites are occupied or accessible.

Figure 3 shows the structures of the following ruthenium dyes:

Dye	Aldrich Prod. No.	Based On
N3	703206	Bipyridine
N719	703214	Bipyridine
Z907	703168	Bipyridine
K19	791415	Bipyridine
C101	791423	Bipyridine
C106	791393	Bipyridine
N749	791245	Terpyridine

The dyes N3, N719, and N749 display hydrophilic behaviors due to the presence of protonated and deprotonated carboxylic acid functionalities of all pyridine-based ligands. The other dyes display hydrophobic behavior, once anchored on TiO<sub>2</sub>, due to the presence of apolar chains on the non-anchoring bipyridine. All bipyridine dyes are charged balanced with respect to the ruthenium ion; the terpyridine dye is, however, anionic due to the presence of three isothiocyanate groups binding the ruthenium metallic center. The bipyridine-based dyes result in shades of red to maroon coloration; the terpyridine dye results in a dark green coloration which can be virtually black for non-transparent devices.

Aliphatic and other apolar side chains containing aromatic, electron rich, and donating moieties result in the following trends:

- Higher extinction coefficients due to the increased size of  $\pi$ -system so that generally lower quantities of dye (and ruthenium) are required per unit area
- Lower recombination, since I<sub>3</sub><sup>-</sup> access to the TiO<sub>2</sub> surface is hindered by size and the dynamic motion of the side groups
- Increased electrostatic binding to the TiO<sub>2</sub> surface due to higher ground state pK<sub>a</sub>
- Decreased charge on the dye attenuating the electrostatic repulsion between adsorbed dye units; thereby increasing the dye loading
- Increased stability of solar cells toward water-induced dye desorption
- Cathodic shift of the oxidation potential of these complexes, compared to that of the N3 sensitizer, which increases the reversibility of the ruthenium III/II couple, leading to enhanced stability<sup>17</sup>

In addition to the above mentioned advantages of extended aliphatic and conjugated side chains, the corresponding metal to ligand charge transfer (MLCT) is also expected to shift to a higher wavelength.<sup>18</sup> The bathochromic effect is mainly controlled by the increase in conjugation

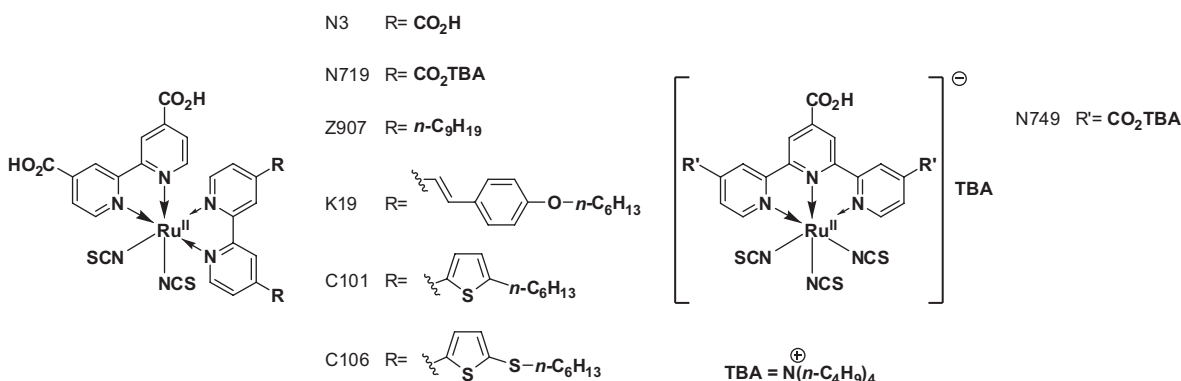


Figure 3. Structures of bi- and terpyridine-based ruthenium dyes.

between pyridines rather than by the lipophilic side chains. Also, modifying the number of conjugated electrons affects the molar absorptivity, which can be observed when comparing the bipyridine-based structures to the terpyridine one in Figure 4; the red shifts are relatively modest when going from N3 to C106 or even K19, as opposed to N3 versus N749.

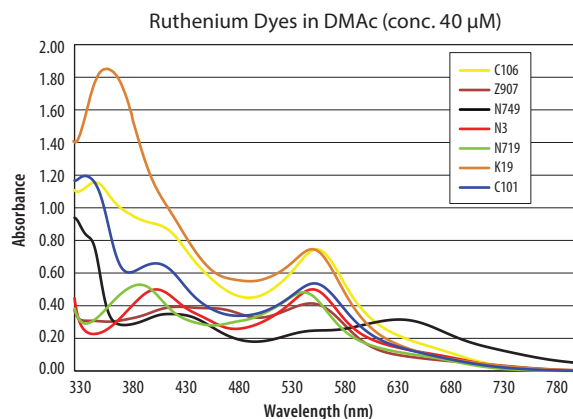


Figure 4. UV-VIS spectra for bi- and terpyridine-based ruthenium dyes.

## Electrolytes

The electrolyte in DSC devices has several important functions:

- Internal charge transport to allow for current flow in an external circuit
  - Dye regeneration following dye excitation and electron injection into TiO<sub>2</sub> according to Equation 4:
- $$\text{Dye}^+ + 3/2 \text{I}^- \rightarrow \text{Dye} + 1/2 \text{I}_3^- \quad (4)$$
- Diffusional equilibration of I<sub>3</sub><sup>-</sup>/I<sup>-</sup> concentration gradients created due to I<sub>3</sub><sup>-</sup> generation at the photoanode and partial I<sub>3</sub><sup>-</sup> depletion at the counter electrode.

Since DSC devices are electrochemical high-power devices with current densities of 20 mA/cm<sup>2</sup> and beyond, adequate electrolyte conductivity and relatively fast diffusion are important for high device efficiency.

**Table 1** compares electrolyte conductivity for EL-HPE (Aldrich Prod. No. 791482), EL-HSE (Aldrich Prod. No. 791466), and EL-HTE (Aldrich Prod. No. 791458). Electrolyte conductivity generally decreases with increasing solvent viscosity and boiling point. It is important to note that direct resistive loss in DSC electrolytes are relatively minor compared to Ohmic loss through the TCO. An electrolyte conductivity of 10 mS/cm in a 1×1 cm cell with an internal gap of 40 μm results in a resistance of only 0.4 Ohm, while TCO resistance would typically be on the order of 10–18 Ohm for the same cell. On the other hand, electrolyte viscosity has a much more serious impact on losses due to concentration polarization, i.e., the establishment of a concentration gradient between anode and cathode.

**Table 1.** Electrolyte Conductivity of Three Benchmark DSC Electrolyte Systems

Electrolyte	Solvent	Conductivity (mS/cm at 20 °C)
EL-HPE (Aldrich Prod. No. 791482)	Acetonitrile	16.5–18.5
EL-HSE (Aldrich Prod. No. 791466)	3-Methoxypropionitrile	8–10
EL-HTE (Aldrich Prod. No. 791458)	3-Butoxypropionitrile	2–4

Additionally, the electrolyte system has to be chemically and photochemically stable up to temperatures of 85 °C and even beyond in very hot climates. Unfortunately, the requirements of performance and stability are often diametrically opposed. High electrolyte conductivity and fast I<sub>3</sub><sup>-</sup> diffusion are generally achieved from solvents with a low viscosity and boiling point, such as acetonitrile. Such electrolyte systems, e.g., EL-HPE, are suitable to demonstrate high cell performance. Acetonitrile-based devices do not, however, offer prolonged stability of device output. For improved long-term stability, solvents with a higher boiling point and viscosity<sup>19</sup> or even ionic liquid-based systems<sup>18,20</sup> are required. Excellent long-term stability has been demonstrated for 100×100 to 150×150 mm DSC devices based on EL-HSE<sup>17</sup> at 85 °C in the dark by the Fraunhofer Institute for Solar Energy System<sup>21</sup> and under light and 85 °C by 3G Solar,<sup>22</sup> respectively.

## Platinum Paste

DSC devices based on the I<sub>3</sub><sup>-</sup>/I<sup>-</sup> redox shuttle require efficient electrochemical regeneration of photochemically produced I<sub>3</sub><sup>-</sup>. Reduction of I<sub>3</sub><sup>-</sup> to 3I<sup>-</sup> is a two-electron transfer process, a rather complex and relatively slow reaction that may involve a number of intermediates.<sup>23</sup> Platinum (Pt) is the most efficient electrocatalyst so far, where quantities of 2–4 μg/cm<sup>2</sup> correspond to an average thickness of 1–2 nm which is sufficient to provide an efficient device and transparency. It has been shown, however, that the most active Pt electrodes for electrochemical I<sub>3</sub><sup>-</sup> reduction are not flat and smooth, but rather based on Pt nanoclusters of ca. 5 nm average size distributed over the TCO surface.<sup>24</sup> Such nanostructured layers can be prepared through thermal decomposition of H<sub>2</sub>PtCl<sub>6</sub> at 380–420 °C.

PT-1 paste (Aldrich Prod. No. 791512) has been formulated for easy and reproducible Pt deposition, primarily on TEC substrates, using high throughput screen printing to provide patterned deposition capabilities. This produces efficient counter electrodes for semitransparent as well as opaque DSC devices.

## Silver Inks

High quality contacts and bus bars are important for minimizing resistive losses from current collection and from contact resistance to the conductive substrate. They are particularly important at higher light levels and for devices with an active area of greater than 1 cm<sup>2</sup>. Another requirement for electrical contacts is solderability for cabling purposes. Silver (due to its very high electrical conductivity, good resistance toward atmospheric corrosion, and favorable solderability) is the material of choice. Because of its high cost, it is important to achieve the specified conductivity at the lowest silver loading. For high-temperature compatible materials, such as for standard photovoltaic silicon wafers, glass frit-based silver pastes are employed, which are processed at temperatures above 500 °C. While such pastes can be used for glass-based DSC, they are not suitable in conjunction with polymer substrates for flexible devices, where polymer-based formulations are required.

The vast majority of polymer thick film (PTF) conductive silver inks consist of silver particles held together by an insulating organic resin or binder mixed with a solvent carrier. The inks can be printed onto a range of substrates using methods such as screen printing, flexographic printing, inkjet, etc., followed by drying in ovens. The drying process essentially removes the carrier solvent and conductivity is achieved as a result of point-to-point contact between the silver particles. However, at lower annealing temperatures (<200 °C), the residual nonconductive binders limit the achievable conductivity. Higher firing temperatures can help burn off residual binders and increase conductivity; however, it can have a detrimental effect on the substrate material and/or to adhesion between substrate and conductive film.

Unlike other conventional inks, DYAG silver inks (Aldrich Prod. Nos. 791873, 791881, and 791903) are formulated to generate nanoscale silver particles as a result of a thermally induced reaction. “Chemically welded” bridges form between silver particles during the thermal process, resulting in a continuous metal track (see **Figure 5**) which provides far superior particle-to-particle contacts compared to conventional inks. This enables DYAG silver inks to achieve higher conductivities at low curing temperatures and low silver content.

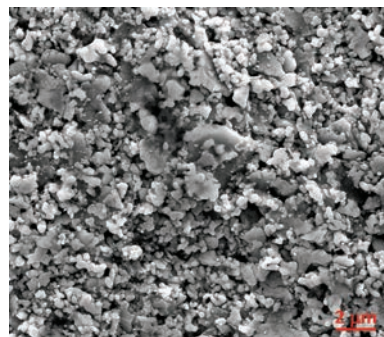


**Figure 5.** SEM of DYAG100 ink after drying and curing.

The DYAG series of inks has been designed to enable outstanding printability and excellent adhesion when applied on a variety of substrates, including polyesters and TCO-coated substrates, making them ideal for both flexible and rigid substrates. **Table 2** shows a range of resistivity and application requirements of DYAG silver inks. These inks are not only suitable for DSC but also for organic PV (OPV) and, generally, for emerging printed electronics applications such as radio frequency identification tags, smart cards, OLEDs, electronic paper, etc., where relatively low temperature curing, combined with high conductivity, flexibility, and reliability are important.

**Table 2.** Properties of DYAG Silver Inks

Silver ink	Specific Resistivity ( $\mu\Omega\text{-cm}$ )	Solid Content (wt %)	Viscosity (Pa.s) at Shear Rate of 10 s <sup>-1</sup> at 25 °C
DYAG 50 (Aldrich Prod. No. 791873)	5–6	80±5	13–17
DYAG 100 (Aldrich Prod. No. 791881)	9–10	80±5	9–12
DYAG 350 (Aldrich Prod. No. 791903)	30–35	70±5	6–9

For more Silver Inks, refer to *page 4*.

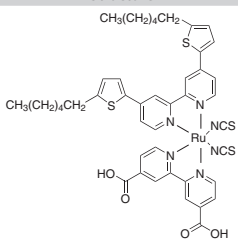
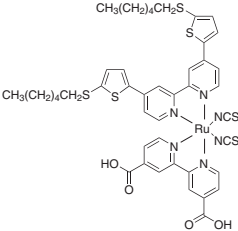
## Conclusions

While individual material optimization is key to achieve high efficiency, for instance maximizing light capture by controlling titania haze and dye extinction coefficient, the interaction of components, particularly the electrolyte, determine system stability. Not only is it important to have a clear understanding of the individual materials and their characteristics, but also being aware of the interactions within the combinations operating in a full DSC system is necessary for delivering the required array of final device properties. The widespread availability of such well-characterized and dependable products will facilitate consistent DSC research and enhance reproducibility and reliability of results. Improved research outputs will contribute to more rapid advances in DSC technology and assist in delivering tangible approaches to tackle future global energy requirements.

## Dyes

### Metal Complex Dyes

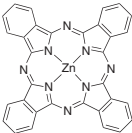
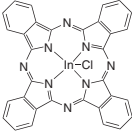
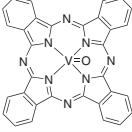
For a complete list of available materials, visit [aldrich.com/dssc](http://aldrich.com/dssc).

Structure	Name	Purity/Dye Content	Absorption	Prod. No.
	C101 Dye	≥95%, H-NMR	$\lambda_{\text{max}}$ 305 nm	791423-250MG
	C106 Dye	≥95%, H-NMR	$\lambda_{\text{abs}}$ 540, 397, 314 nm 0.02 mM in ethanol	791393-250MG

### References

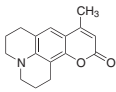
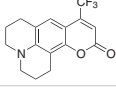
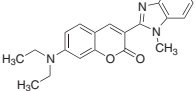
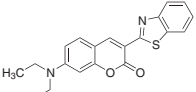
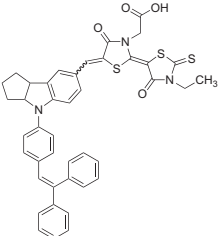
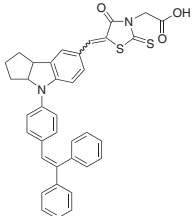
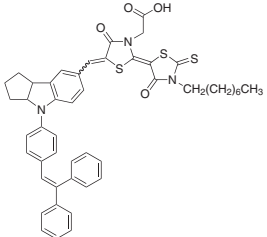
- McEvoy, A.J., Grätzel, M. *Sol. Energy Mater. Sol. Cells* **1994**, 32, 221.
- Gerischer, H., Michel-Beyerle, M.E., Rebentrost, F., Tributsch, H. *Electrochim. Acta* **1968**, 13, 1515.
- Desilvestro, J., Grätzel, M., Kavan, L., Moser, J., Augustynski, J. *J. Amer. Chem. Soc.* **1985**, 107, 2988.
- Patent: WO1991016719.
- O'Regan, B., Grätzel, M. *Nature* **1991**, 353, 737.
- Desilvestro, H. Dyesol, [http://www.dyesol.com/media/wysiwyg/Documents/media-centre/Unique\\_Characteristics\\_and\\_Benefits\\_of\\_DSC.pdf](http://www.dyesol.com/media/wysiwyg/Documents/media-centre/Unique_Characteristics_and_Benefits_of_DSC.pdf) (accessed November 2013).
- Yella, A., Lee, H.-W., Tsao, H.N., Yi, C., Chandiran, A.K., Nazeeruddin, M.K., Diao, E.W.-G., Yeh, C.-Y., Zakeeruddin, S.M., Grätzel, M. *Science* **2011**, 334, 629.
- Burschka, J., Pellet, N., Moon, S.-J., Humphry-Baker, R., Gao, P., Nazeeruddin, M.K., Grätzel, M. *Nature* **2013**, 499, 316.
- Milliken, D., Desilvestro, H. [http://www.dyesol.com/media/wysiwyg/Documents/dsc-resource-library/Solid\\_or\\_Liquid\\_-\\_July\\_2013.pdf](http://www.dyesol.com/media/wysiwyg/Documents/dsc-resource-library/Solid_or_Liquid_-_July_2013.pdf) (accessed November 2013).
- Braun, J.H. *J. Coating Technol.* **1990**, 62, 37.
- Coletti, G. *Prog Photovolt Res Appl.* **2013**, 21, 1163.
- Ohtani, B., Prieto-Mahoney, O.O., Li, D., Abe, R. *J. Photochem. Photobiol. A Chem.* **2010**, 216, 179.
- Chiba, Y., Islam, A., Watanabe, Y., Komiya, R., Koide, N., Han, L. *Jpn. J. Appl. Phys.* **2006**, 45, L638.
- Zakeeruddin, S.M., Grätzel, M. *Adv. Funct. Mater.* **2009**, 19, 2187.
- Zhao, D., Peng, T., Lu, L., Cai, P., Jiang, P., Bian, Z. *J. Phys. Chem. C.* **2008**, 112, 8486.
- Shklover, V., Ovchinnikov, Y.E., Braginsky, L.S., Zakeeruddin, S.M., Grätzel, M. *Chem. Mater.* **1998**, 10, 2533.
- Klein, C., Nazeeruddin, M.K., Di Censo, D., Liska, P., Grätzel, M. *Inorg. Chem.* **2004**, 43, 4216.
- Hirata, N., Lagref, J.J., Palomares, E.J., Durrant, J.R., Nazeeruddin, M.K., Grätzel, M., Di Censo, D. *Chem. Eur. J.* **2004**, 10, 595.
- Jiang, N., Sumitomo, T., Lee, T., Pellaroque, A., Bellon, O., Milliken, D., Desilvestro, H. *Sol. Energy Mater. Sol. Cells* **2013**, 36, 119.
- Harikisun, R., Desilvestro, H. *Sol. Energy* **2013**, 85, 1179.
- Hinsch, A., Veurman, W., Brandt, H., Loayza Aguirre, R., Bialecka, K., Flarup Jensen, K. *Prog. Photovoltaics Res. Appl.* **2011**, 20, 698.
- Goldstein, J., Yakupov, I., Breen, B. *Sol. Energy Mater. Sol. Cells* **2010**, 94, 638.
- Boschloo, G., Hagfeldt, A. *Accounts Chem. Res.* **2009**, 42, 1819.
- Papageorgiou, N., Maier, W.F., Grätzel, M. *J. Electrochem. Soc.* **1997**, 144, 876.

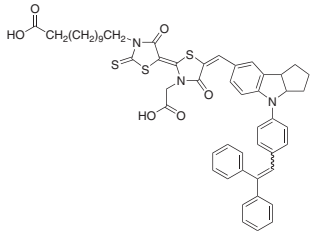
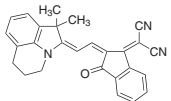
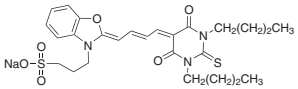
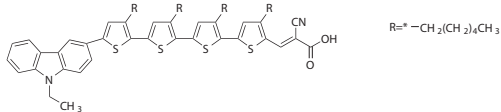
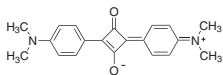
Structure	Name	Purity/Dye Content	Absorption	Prod. No.
	K19 Dye	≥95%, H-NMR	$\lambda_{\text{abs}}$ 536, 357, 311 nm 0.02 mM in DMF	791415-250MG
	<i>cis</i> -Bis(isothiocyanato)bis(2,2'-bipyridyl-4,4'-dicarboxylato)ruthenium(II)	95%, NMR	$\lambda_{\text{abs}}$ 534, 395, 312 nm	703206-250MG 703206-1G
	Di-tetrabutylammonium <i>cis</i> -bis(isothiocyanato)bis(2,2'-bipyridyl-4,4'-dicarboxylato)ruthenium(II)	Dye content ≥ 90% (HPLC), 95%, NMR	$\lambda_{\text{abs}}$ 534, 393, 313 nm	703214-250MG 703214-1G
	N749 Black Dye	≥95%, H-NMR	$\lambda_{\text{abs}}$ 615, 415, 341, 329 nm 0.02 mM in ethanol	791245-100MG 791245-250MG
	<i>cis</i> -Bis(isothiocyanato)(2,2'-bipyridyl-4,4'-dicarboxylato)(4,4'-di-nonyl-2'-bipyridyl)ruthenium(II)	Dye content ≥ 90%, 95%, NMR	$\lambda_{\text{abs}}$ 531, 314, 295 nm	703168-250MG 703168-1G
	Titanylphthalocyanine, type I	Dye content > 99%	$\lambda_{\text{max}}$ 700 nm	791849-1G
	Titanyl phthalocyanine	Dye content 95%	$\lambda_{\text{max}}$ 692 nm	404551-1G
	Copper(II) phthalocyanine	>99.95% trace metals basis, triple-sublimed grade	$\lambda_{\text{max}}$ 678 nm	702854-500MG
	Copper(II) phthalocyanine	Dye content 99%, sublimed grade	$\lambda_{\text{max}}$ 678 nm	546674-1G 546674-5G
	Copper(II) phthalocyanine	Dye content > 99%	$\lambda_{\text{max}}$ 678 nm	546682-200MG 546682-2G
	Copper(II) phthalocyanine	Dye content 90%	$\lambda_{\text{max}}$ 678 nm	252980-5G 252980-25G 252980-100G
	Tin(IV) 2,3-naphthalocyanine dichloride	99%	$\lambda_{\text{max}}$ ~875 nm	757330-250MG

Structure	Name	Purity/Dye Content	Absorption	Prod. No.
	Zinc phthalocyanine	Dye content 97%	$\lambda_{\max}$ 701 nm	341169-5G 341169-25G
	Indium(III) phthalocyanine chloride	Dye content > 95%	$\lambda_{\max}$ 697 nm	791857-1G
	Vanadyl phthalocyanine	Dye content > 90%	$\lambda_{\max}$ 701 nm	791997-500MG

## Metal-free Dyes

For a complete list of available materials, visit [aldrich.com/dssc](http://aldrich.com/dssc).

Structure	Name	Purity/Dye Content	Absorption	Prod. No.
	Coumarin 102	Dye content 99%	$\lambda_{\max}$ 390 nm	546151-100MG
	Coumarin 153	Dye content 99%	$\lambda_{\max}$ 422 nm	546186-100MG
	Coumarin 30	Dye content 99%	$\lambda_{\max}$ 413 nm	546127-100MG
	Coumarin 6	≥99%	$\lambda_{\max}$ 443 nm	546283-100MG
	D149 Dye	98%, HPLC	$\lambda_{\max}$ 531 nm	736015-100MG
	D102 Dye	95%, HPLC	$\lambda_{\max}$ 499 nm in DMF	745944-200MG
	D205 Dye	97%, HPLC	$\lambda_{\text{abs}}$ 531, 392 nm	745618-100MG

Structure	Name	Purity/Dye Content	Absorption	Prod. No.
	D358 Dye	-	$\lambda_{\max}$ 532 nm in DMF	746606-100MG
	Merocyanine dye, HB194	-	$\lambda_{\max}$ ~578 nm in dichloromethane	747211-250MG
	Merocyanine 540	Dye content 90%	$\lambda_{\max}$ 555 nm	323756-100MG
	MK-2 Dye	95%	-	728705-100MG
	1,3-Bis[4-(dimethylamino)phenyl]-2,4-dihydroxycyclobutenediylum dihydroxide, bis(inner salt)	Dye content 90%	$\lambda_{\max}$ 625 nm	149063-1G

## Nanoparticles

For a complete list of available materials, visit [aldrich.com/dssc](http://aldrich.com/dssc).

Name	Form	Particle Size (nm)	Prod. No.
Titanium(IV) oxide, anatase	nanopowder	<25	637254-50G 637254-100G 637254-500G
Titanium(IV) oxide, mixture of rutile and anatase	nanopowder	<100 (BET)	634662-25G 634662-100G
	nanoparticles paste	~21 (primary particle size of starting nanopowder) <250 (DLS)	700355-25G
	dispersion nanoparticles	~21 (primary particle size of starting nanopowder) <150 (DLS)	700347-25G 700347-100G
Titanium(IV) oxide, rutile	nanopowder	<100	637262-25G 637262-100G 637262-500G
Zinc oxide	nanopowder	<100	544906-10G 544906-50G
	nanopowder	<50 (BET)	677450-5G

## Pastes

For a complete list of available materials, visit [aldrich.com/dssc](http://aldrich.com/dssc).

Name	Composition	Particle Size	Prod. No.
Silver	≥ 75%	particle size <5 nm (20%) particle size 200 nm (80%)	735825-25G
Titania paste, transparent	19.0 wt. %	20 nm	791547-10G 791547-20G
		avg. part. size ≤450 nm (scatter) avg. part. size 20 nm (active)	791555-5G 791555-20G
Titania paste, reflector	20.0 wt. %	150 - 250 nm	791539-5G 791539-20G
Platinum paste, screen printable	-	-	791512-20G

## Electrolytes

For a complete list of available materials, visit [aldrich.com/dssc](http://aldrich.com/dssc).

Name	Form	Conductivity (mS/cm)	Prod. No.
EL-HSE high stability electrolyte	liquid	8-10 at 20 °C	<a href="#">791466-10ML</a> <a href="#">791466-50ML</a>
EL-HTE high temperature electrolyte	liquid	2-4 at 20 °C	<a href="#">791458-5ML</a> <a href="#">791458-25ML</a>
EL-HPE high performance electrolyte	liquid	16.5-18.5 at 20 °C	<a href="#">791482-10ML</a> <a href="#">791482-50ML</a>

## Organic Hole Conductors

For a complete list of available materials, visit [aldrich.com/dssc](http://aldrich.com/dssc).

Structure	Name	Description	Prod. No.
	Spiro-MeOTAD	$\lambda_{\text{abs}}$ 385, 306 nm in dichloromethane	<a href="#">792071-1G</a>
	2,2',7',7'-Tetrakis(N,N-diphenylamino)-9,9-spirobifluorene	99%, HPLC absorption 378 $\mu\text{m}$ in THF	<a href="#">765007-1G</a>
	Poly(3-hexylthiophene-2,5-diyl)	99.995% trace metals basis electronic grade average $M_n$ , 54,000-75,000 (>98% head-to-tail regioregular (HNMR)) regioregular	<a href="#">698997-250MG</a> <a href="#">698997-1G</a> <a href="#">698997-5G</a>
	Poly(3-hexylthiophene-2,5-diyl)	99.995% trace metals basis electronic grade average $M_n$ , 15,000-45,000 (>95% head-to-tail regioregular (HNMR)) regioregular	<a href="#">698989-250MG</a> <a href="#">698989-1G</a> <a href="#">698989-5G</a>
	Poly(3-hexylthiophene-2,5-diyl)	regioregular	<a href="#">445703-1G</a>
	Poly(3-hexylthiophene-2,5-diyl)	regiorandom	<a href="#">510823-1G</a>
	Polypyrrole	composite with carbon black doped proprietary organic sulfonic acid as dopant	<a href="#">530573-25G</a>
	Polypyrrole	proprietary organic sulfonic acid as dopant	<a href="#">577030-5G</a> <a href="#">577030-25G</a>
	Polypyrrole	coated on titanium dioxide doped proprietary organic sulfonic acid as dopant	<a href="#">578177-10G</a>
	Polypyrrole	5 wt % dispersion in H <sub>2</sub> O doped proprietary organic acids as dopant	<a href="#">482552-100ML</a>
	Polypyrrole-block-poly(caprolactone)	0.3-0.7 wt. % (dispersion in nitromethane) <i>p</i> -toluenesulfonate as dopant	<a href="#">735817-25G</a>
	Polyaniline (emeraldine salt)	composite (20 wt.% polyaniline on carbon black) proprietary organic sulfonic acid	<a href="#">530565-5G</a> <a href="#">530565-25G</a>
	Polyaniline (emeraldine salt)	composite (30 wt.% polyaniline on nylon)	<a href="#">577073-10G</a>
	Polyaniline (emeraldine salt) short chain, grafted to lignin	-	<a href="#">561126-10G</a>

# DEVELOPMENT OF SMALL MOLECULE DONORS FOR SOLUTION-PROCESSED ORGANIC SOLAR CELLS



Abby-Jo Payne and Gregory C. Welch  
Dalhousie University, Department of Chemistry  
6274 Coburg Road, Halifax, Nova Scotia, Canada B3H 4R2  
Email: gregory.welch@dal.ca

## Introduction

Solution-processed organic photovoltaic devices (OPVs) have emerged as a promising clean energy generating technology due to their ease of fabrication, potential to enable low-cost manufacturing via printing or coating techniques, and ability to be incorporated onto light weight, flexible substrates.<sup>1</sup> The most successful class of OPV devices are those with active layers composed of blended polymeric electron donors and fullerene acceptors, widely known as polymer–fullerene bulk heterojunction (BHJ) solar cells.<sup>2</sup> Power conversion efficiencies (PCE) for these systems have reached 9.2% for single-layer devices<sup>3</sup> having already shown great promise as renewable, lightweight and low-cost energy sources. Recently, the power-conversion efficiency of state-of-the-art PSCs has exceeded 8% in the scientific literature. However, to find viable applications for this emerging photovoltaic technology, further enhancements in efficiency will be required to increase efficiency and achieve the required performance threshold (10% for commercial applications and 10.6% for tandem cells).<sup>4</sup>

Recently, several new classes of small molecule donors with favorable optical and electronic properties have been reported for use in OPV devices.<sup>5,6</sup> These small molecules offer advantages over their polymeric counterparts: (a) their structures are well defined and exhibit no molecular weight dependence, leading to improved purity and limiting batch-to-batch variation; and (b) they typically exhibit more organized nanostructures, leading to higher charge carrier mobilities. Additionally, small molecule architectures are sensitive to subtle structure changes; thus, electronic energy levels, optical absorption, and self-assembly tendencies can be systemically tuned to maximize device performance. When coupled with fullerene electron acceptors such as [6,6]-phenyl-C<sub>71</sub>-butyric acid methyl ester (PC<sub>71</sub>BM) (Aldrich Prod. No. 684465), small molecule-based solar cells have achieved record PCEs over 8%.<sup>7,8</sup> This article highlights the progress of small molecule-based organic solar cells over the past few years and describes key structural features that have led to this performance improvement.

## Device Operation and Donor Molecular Design

While a detailed analysis of photocurrent generation in OPVs<sup>1-3</sup> is beyond the scope of this article, it is important to recognize that organic solar cells operate on the principle that two materials are required to generate free charge carriers. A simplified view of device operation is shown in **Figure 1A**. Combinations of materials with high ionization potentials (electron *donor*) and high electron affinity (electron *acceptor*) are responsible for light absorption, exciton formation, charge separation, and charge transport. Ubiquitous to OPV devices is the use

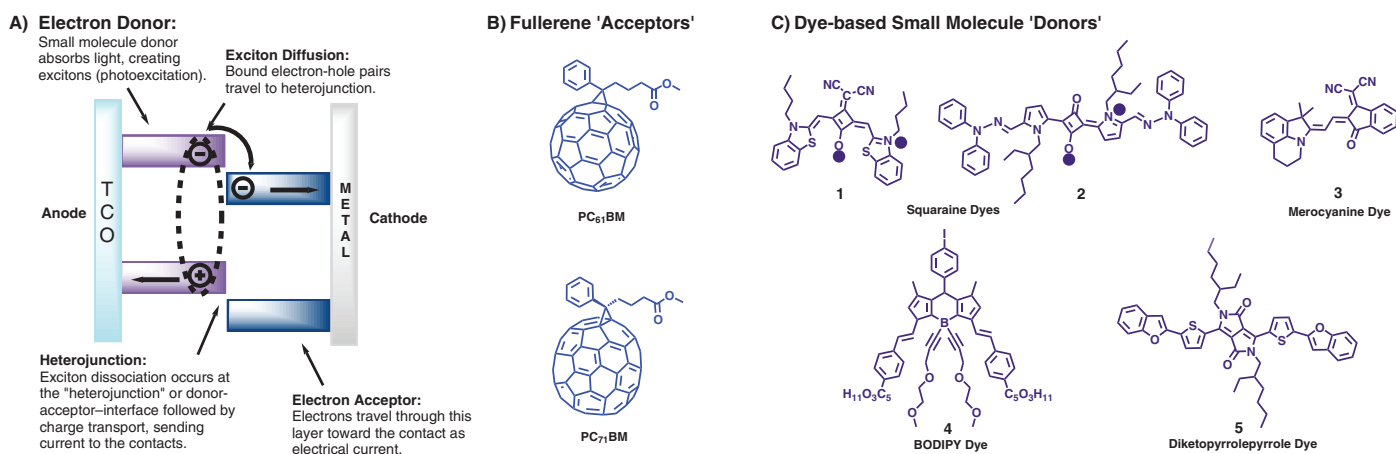


**Figure 1.** A) Simplified figure showing organic solar cells device operation (TCO = transparent conducting oxide). Chemical structures of **B)** commonly used soluble fullerene derivatives, and **C)** early examples of small molecule donors constructed from common organic dyes.

of soluble fullerene derivatives as the electron acceptor owing to their low lying, lowest unoccupied molecular orbital levels and isotropic electron mobility (Figure 1B). The vast majority of OPV performance improvements has been a result of the development of new 'donor' materials that are designed to maximize light absorption, transport charge, and form ordered nanostructures when blended with fullerenes. While  $\pi$ -conjugated polymers have received the most attention, small molecules can be strategically designed for use as effective 'donor' materials.

There are several key parameters to consider when designing small molecule donors to be paired with fullerene acceptors in solution-processed BHJ solar cells, including: (a) strong optical absorption that extends into the near-IR region ( $\lambda_{\text{max}}$  should be centered around 700 nm, the region of maximum photon flux) and extinction coefficients ( $\epsilon$ ) greater than  $50,000 \text{ M}^{-1} \text{ cm}^{-1}$  are desired to maximize photon harvesting; (b) relatively deep highest occupied molecular orbital (HOMO) energy levels from  $-5$  to  $-5.5 \text{ eV}$  to maximize open circuit voltages, while still matching commonly used high work function anodes; (c) relatively planar structures to promote intermolecular  $\pi$ - $\pi$  interactions which are important for achieving high charge carrier mobility; (d) sufficient solution viscosity and solubility to enable thin film formation via solution deposition; and (e) synthetic procedures that are simple, high yielding, and highly tunable to ensure both gram quantities can be made and molecular libraries can be created. With these considerations in mind, several research groups have developed a series of solution-processable small molecules that challenge those of the very best polymers in solar cell applications.

## Initial Donor Small Molecules

The development of high-performance solution-processed small molecule bulk heterojunction solar cells (SM-BHJ) did not happen overnight. Rather, there has been a long history of work in the area coming from a few research groups. Historically, small molecule donors have tended to be just that, small. They exhibited difficulties in forming uniform thin films from solution and, thus, have primarily been utilized in thermally evaporated devices.<sup>9</sup> In the mid-2000s, Roncali *et al.* developed a series of tetrahedral-shaped oligothiophene molecular donors that could be solution-processed with  $\text{PC}_{61}\text{BM}$  to produce solar cells with a PCE of  $\sim 0.2\%$ .<sup>10</sup> Around the same time, Anthony *et al.* reported a series of soluble acene derivatives which achieved PCEs of  $\sim 1\%$  when paired with  $\text{PC}_{61}\text{BM}$ .<sup>11</sup> A major problem with these initial compounds was poor spectral overlap with the solar spectrum and limited optical absorption beyond 600 nm. None-the-less, these initial results demonstrated that small molecule donors could indeed be processed from solution to give working solar cell devices. Overcoming the issue of poor light harvesting properties, a series of papers was published between 2008 and 2010 describing the functionalization of strongly absorbing dyes. Zeisel and Roncali showed that highly absorbing ( $\epsilon > 100,000 \text{ M}^{-1} \text{ cm}^{-1}$ ) BODIPY dyes (Aldrich Prod. Nos. 745820, 746169, 747106, and 790389) could be made soluble and form films from solution by attaching oligoxyethylene chains to the  $\pi$ -conjugated backbone. When incorporated into devices with  $\text{PC}_{61}\text{BM}$ , PCEs in excess of 1% were obtained and, most importantly, photo-current generation beyond 750 nm was achieved.<sup>12</sup> The PCE of BODIPY-based SM-BHJ solar cells has since been improved to  $\sim 5\%$ .<sup>13</sup> Both Marks<sup>14</sup> and Würthner<sup>15</sup> research groups reported on functionalized squaraine dyes (Aldrich Prod. Nos. 757233, 757268, 757276, and 758337) that exhibited broad and intense thin film absorption spectra extending well into the near IR. Devices with  $\text{PC}_{61}\text{BM}$  gave PCEs on the

order of 1–2%. These devices ultimately suffered from small open circuit voltages ( $V_{\text{oc}}$ ) and poor fill factors, a result of high-lying HOMO levels and poor active layer morphologies.

Würthner also successfully incorporated merocyanine dyes (Aldrich Prod. No. 323756) into BHJ solar cells. Such dyes are easily synthesized and exhibited strong absorption in the red region of the solar spectrum. PCEs upward of 2.5% were obtained upon solution-processing the dye with soluble fullerene derivatives.<sup>16</sup> These devices had a higher  $V_{\text{oc}}$  in comparison to the squaraine-based devices, yet once more suffered from poor fill factors. In the late 2000s, Nguyen *et al.* utilized the strongly absorbing diketopyrrolopyrrole dye (Aldrich Prod. Nos. 753912 and 753920) to construct a series of narrow band gap, solution-processable small molecules for use in OPV devices. One such derivative incorporated 2-ethylhexyl alkyl chains on the amide N-atom to enable dissolution in organic solvents and 2-benzofuran units on the terminal positions to extend  $\pi$ -delocalization and direct self-assembly. This molecule, named  $\text{DPP}(\text{ThBzFu})_2$ , had near ideal optical and electronic properties for use as a donor molecule in SM-BHJ solar cells, including strong optical absorption beyond 700 nm, a deep HOMO level, and a simple three-step synthesis from commercially available starting materials. Solar cells fabricated with  $\text{DPP}(\text{ThBzFu})_2:\text{PC}_{71}\text{BM}$  active layers yielded PCEs in excess of 4%, a record that stood for two years.<sup>17</sup> Important parameters for achieving such a high PCE were the use of high concentrations of  $\text{DPP}(\text{ThBzFu})_2$  compared to  $\text{PC}_{71}\text{BM}$  and thermal annealing of the active layer to achieve appropriate nanoscale phase separation, thus indicating the importance of active layer processing. Ultimately, this initial work on soluble small molecule donors by Roncali, Anthony, Marks, Würthner, Nguyen and others set the stage for major breakthroughs in subsequent years. Three excellent reviews by Nguyen<sup>18</sup>, Baurele<sup>19</sup>, and Zhan<sup>20</sup> provide a more detailed analysis of the field.

## High-performance Donor Small Molecules

Building on the established literature, and taking into account the specific criteria to develop small molecule donors, Heeger and Bazan reported on a highly modular molecular framework found to yield materials with near ideal properties for use as donor molecules in BHJ solar cells.<sup>5,21</sup> The architecture consisted of an *acceptor-donor-acceptor* (ADA) core flanked with *end-capping units*. Two acceptors were utilized to increase the electron affinity across the conjugated backbone ensuring deep HOMO levels, while end-capping units served to extend  $\pi$ -conjugation and tailor self-assembly properties. Important to this class of compounds was the use of a pyridyl[2,1,3]thiadiazole (PT) building block as the electron acceptor, which promoted strong intramolecular charge transfer when coupled with electron donors, resulting in narrow band gaps. Additionally, the asymmetrical nature imparted selective reactivity, allowing for the synthesis of monofunctionalized materials in high yield.

Two synthetic entries into this class of compounds are shown in Figure 2A. In Method 1, small molecules are built from the inside out, leading to a final architecture where the pyridyl N-atoms are in a position *proximal* to the donor core; in Method 2, small molecules are built from the outside in, leaving the pyridyl N-atoms in a position *distal* to the donor core. Through these simple three-step syntheses, a whole series of small molecules were made incorporating a range of donor cores and end capping units (Figure 2B). Among the many derivatives synthesized, it was found that utilizing a 2-ethylhexyl-substituted dithienosilole (DTS) *donor* and 2-hexylbithiophene *end-capping units* resulted in virtually ideal optical and electronic properties. The compound *d*-DTS(PTT)<sub>2</sub> (**6**) shown

in **Figure 2C** exhibited strong long wavelength absorption with peak absorption at 700 nm in the solid state (near the region of max photon flux) and HOMO and LUMO levels at  $-5.2$  eV and  $-3.6$  eV, respectively, making it compatible with fullerene derivatives. High organic solvent solubility ( $>20$  mg/mL), as a result of alkyl side chains both perpendicular and parallel to the molecular backbone, allows for uniform film formation. In addition, the planarity of the small molecule, important for intramolecular  $\pi$ -delocalization and intermolecular  $\pi$ -stacking, resulted in high charge carrier mobilities on the order of  $0.1$  cm $^{-1}$  V/s. Incorporating *d*-DTS(PTT) $_2$  into BHJ devices with PC $_{71}$ BM produced initial PCEs of 3.2%. By optimizing device architecture and processing conditions, PCEs were improved to 5.6% through the use of molybdenum oxide (Aldrich Prod. No. 203815) hole transport layers and processing with small amounts of 1,8-diiodooctane (DIO) (Aldrich Prod. No. 250295). To further improve device performance, Bazan and co-workers employed the regio-isomer *p*-DTS(PTT) $_2$  [or *p*-DTS(PTTh) $_2$ , Aldrich Prod. No. 772372, (**7**)], where the pyridyl N-atoms are positioned proximal to the central DTS unit. A slight

change in the molecular geometry toward a more 'banana' shape, resulted in a greater tendency for *p*-DTS(PTT) $_2$  to self-assemble, leading to higher hole mobilities, increased light absorption, and ultimately a higher PCE of 6.7%.<sup>21</sup> This result represented, for the first time, a solution-processed small molecule BHJ device comparable in PCE to its polymer counterparts. Additionally, replacing the pyridyl N-atom for a C-F bond *p*-DTS(FBPTT) $_2$  [or *p*-DTS(FBPTTh) $_2$ , Aldrich Prod. No. 772380, (**8**)], improved the stability of the compound and resulted in PCEs in excess of 7% when processed under the same conditions. Further device optimization has led to PCEs approaching 9%.<sup>7</sup> Quite interestingly, analogous molecules utilizing the ubiquitous benzo[2,1,3]thiadiazole acceptor, compound **9**, exhibited no photovoltaic behavior when processed under similar conditions due to an inability of **9** to form ordered nanostructures required for rapid charge transport.<sup>5</sup> These results highlighted how subtle alterations to molecular structure can greatly impact self-assembly processes and, in turn, device performance.

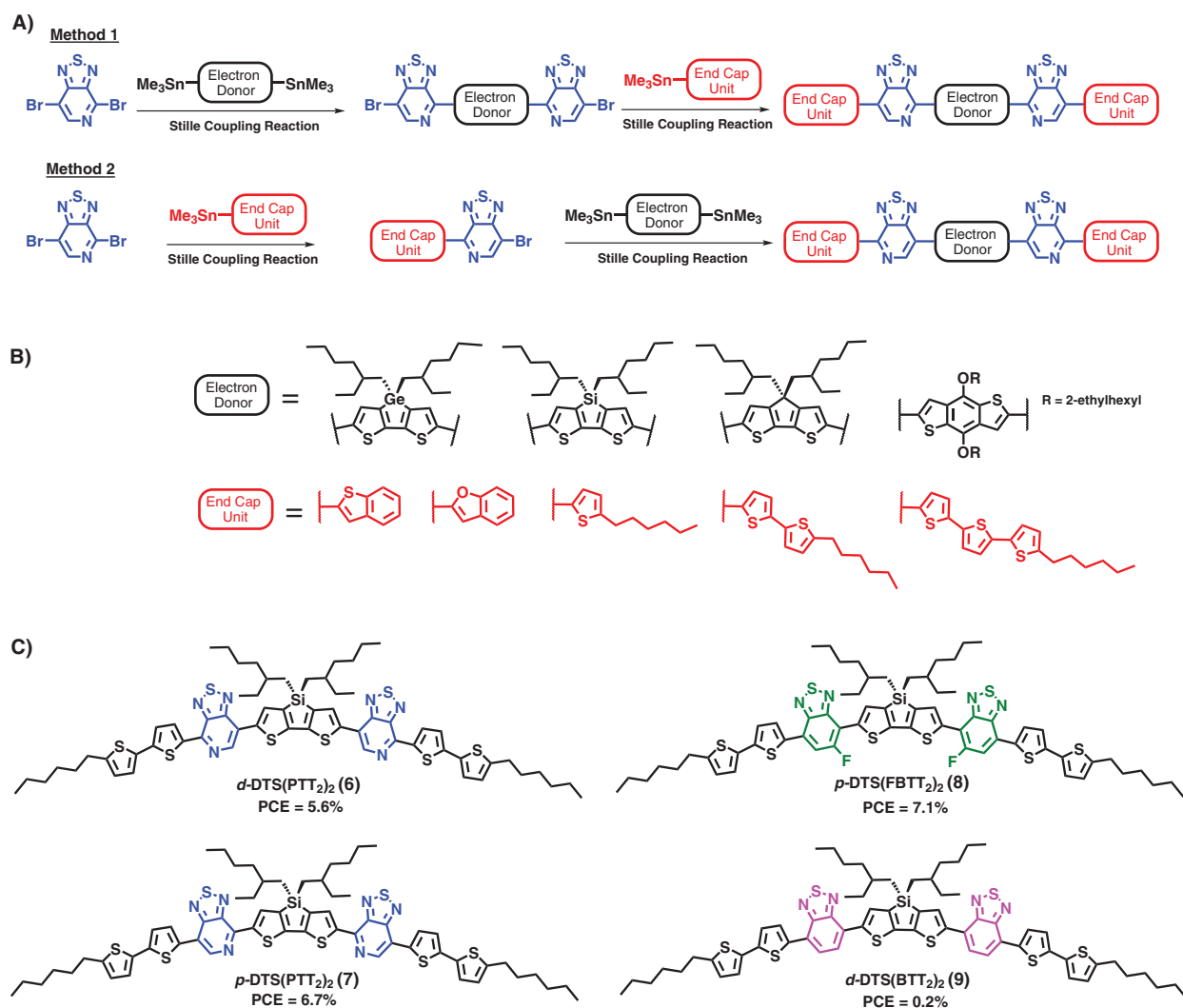


**Figure 2.** Chemical structures of soluble small molecule donors reported by Bazan and co-workers. **A)** General three-step synthetic pathway toward end-capped ADA-type molecules with proximal (Method 1) and distal (Method 2) regio-chemistry of the pyridyl N-atom. **B)** Examples of building blocks used as donors and end caps. **C)** Best performing architecture showing the influence of heteroatom substitution on power conversion efficiency.

In a parallel development, Chen *et al.* reported a series of narrow band gap oligothiophenes that exhibited excellent performance when incorporated into SM-BHJ solar cells.<sup>6</sup> They demonstrated that end capping long septithiophenes with electron withdrawing units provided materials with absorption profiles extending into the red region of the solar spectrum and deep HOMO levels desired to give large  $V_{oc}$ . Critical to these materials was the incorporation of long alkyl side chains on six of the thiophene units which rendered the compounds highly soluble in common organic solvents and enabled the formation of uniform thin films from solution. Initial derivatives with dicyanovinyl end-cap units (**Figure 3A, 10**) were incorporated in BHJ solar cells with PC<sub>61</sub>BM, yielding devices with PCEs of 2.5%, which were further improved to 3.7% with device optimization. Through a systematic screening of end-capping units, Chen *et al.* showed that absorption profiles, HOMO/LUMO levels, and material solubility could be readily tuned. Small molecules incorporating 1,3-dimethylpyrimidine-2,4,6-(1H,3H,5H)-trione (**11**), indan(1,3)dione (**12**), *n*-octyl cyanoacetate (**13**), and 3-ethylrhodanine (**14**) as end capping units gave the best performance with PCEs ranging from 4–6%. Solar cells based on **12** and PC<sub>61</sub>BM had extremely high fill factors of 72% due to the strong tendency for the indan(1,3)dione moiety to direct self-assembly. Compound **12** exhibited a remarkably high solubility in chloroform at >200 mg/mL, which is important for forming thicker films (>300 nm) required for large-scale fabrication. Overall, compound **14** with 3-ethylrhodanine end-capping units exhibited a good combination of high organic solvent solubility and, thus, good film forming properties and long wavelength absorption, leading to the highest PCE of the series. Replacement of the central thiophene ring in **14** with the larger and more rigid benzobithiophene conjugated unit led to compounds with improved charge transport properties resulting in increased device performance (PCE=7.4% for compound **15**). Increasing the  $\pi$ -conjugation orthogonal to the backbone improved photocurrent generation and, with the use of a polydimethylsiloxane (PDMS) (Aldrich Prod. Nos. 423785, 482064, and 482145) processing additive, achieved record PCEs of 8.1%.<sup>8</sup> These findings brought great attention to the area and helped establish solution-processed SM-BHJ solar cells as one of the most promising clean energy technologies.

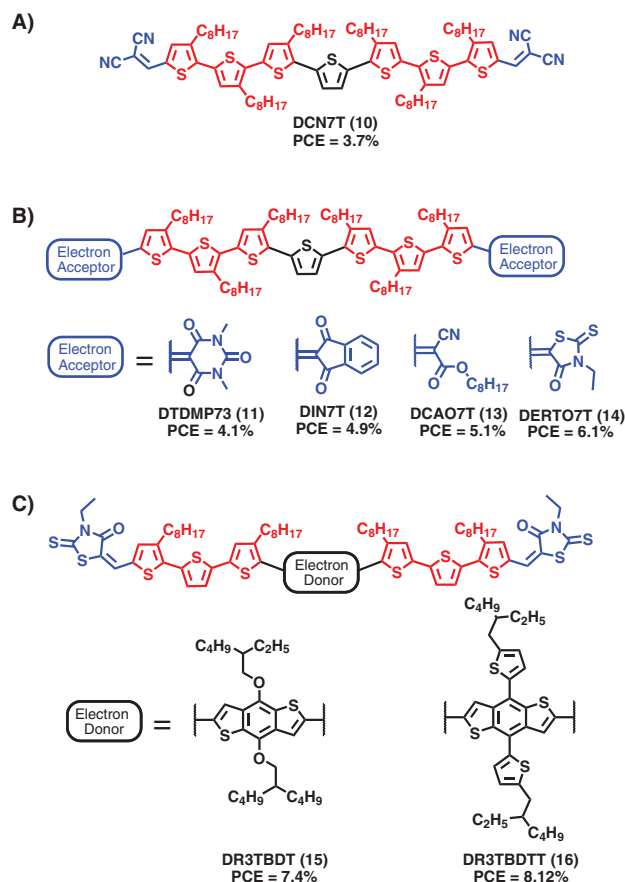


**Figure 3.** Chemical structures of soluble small molecule donors reported by Chen and co-workers.<sup>6</sup> **A)** First generation structure consisting of a septithiophene core end-capped with dicyanovinyl units. **B)** Evolution of terminal end-capping units to give high performance materials. **C)** Small molecules with benzobithiophene based  $\pi$ -conjugated core units yielding best performing materials.

**ALDRICH**  
Materials Science

Now Available for Your iPad<sup>®</sup>

**Material Matters**

Download our free app!  
[aldrich.com/mm](http://aldrich.com/mm)

## Conclusions and Future Outlook

Over the past four years, creative molecular design of small molecule donors has led to a near doubling of the power conversion efficiency of solution-processed small molecule solar cells, with improvements from ~4 to ~8% (Figure 4A). Bazan and Chen's work demonstrated that in addition to the initial design principles, small molecule donors should be constructed with greater than six  $\pi$ -conjugated units in the molecular backbone and decorated with sufficient numbers of alkyl side chains to ensure good solubility and uniform film formation from solution. In each case of high-performance donors, it should be noted not one molecule but rather a large series of compounds were synthesized and evaluated on their structure-property-function relationships; thus, the importance of a highly tunable synthesis cannot be overvalued. Since the report of PCEs in excess of 6% in 2012, the number of publications focused on the development of small molecule donors has increased exponentially (Figures 4B and 4C), with now numerous reports of devices giving PCEs in the range of 5–6%. As a final comment, while the spotlight has recently been directed on small molecule donors, an emerging area of interest is in the design and synthesis of linear donor-acceptor small molecule acceptors to replace fullerenes in BHJ solar cells.<sup>22</sup> Such molecules can be pieced together from the current stock of building blocks used to construct high-performance donors and offer the potential of cost-efficient synthesis, photochemical stability, and increased photon harvesting (Figure 5). Efficiencies have reached 4% to date and are expected to continue to increase. It is fully expected that with the larger number of researchers in the field, and the wide range of building blocks available, a 10% efficient, solution-processed, all small molecule solar cell will be reported in the not-too-distant future.

## Acknowledgments

Dalhousie University, NSERC, and the Canada Research Chairs program are thanked for financial support.

### References

- (1) Su, Y.-W., Lan, S.-C., Wei, K.-H. *Mater. Today* **2012**, *15*, 554.
- (2) Li, G., Zhu, R., Yang, Y. *Nat. Photonics* **2012**, *6*, 153.
- (3) He, Z., Zhong, C., Su, S., Xu, M., Wu, H., Cao, Y. *Nat. Photonics* **2012**, *6*, 591.
- (4) You, J., Dou, L., Yoshimura, K., Kato, T., Ohya, K., Moriarty, T., Emery, K., Chen, C.-C., Gao, J., Li, G., Yang, Y. *Nat. Commun.* **2013**, *4*, 1446.
- (5) Coughlin, J.E., Henson, Z.B., Welch, G.C., Bazan, G.C. *Accounts Chem. Res.* **2013**, DOI: 10.1021/ar400136b.
- (6) Chen, Y., Wan, X., Long, G. *Accounts Chem. Res.* **2013**, DOI: 10.1021/ar400088c.
- (7) Gupta, V., Kyaw, A.K.K., Wang, D.H., Chand, S., Bazan, G.C., Heeger, A.J. *Sci. Reports* **2013**, *3*.
- (8) Zhou, J., Zuo, Y., Wan, X., Long, G., Zhang, Q., Ni, W., Liu, Y., Li, Z., He, G., Li, C., Kan, B., Li, M., Chen, Y. *J. Am. Chem. Soc.* **2013**, *135*, 8484.
- (9) Chen, Y.-H., Lin, L.-Y., Lu, C.-W., Lin, F., Huang, Z.-Y., Lin, H.-W., Wang, P.-H., Liu, Y.-H., Wong, K.-T., Wen, J., Miller, D.J., Darling, S.B. *J. Am. Chem. Soc.* **2012**, *134*, 13616.
- (10) Karpe, S., Cravino, A., Frère, P., Allain, M., Mabon, G., Roncali, J. *Adv. Funct. Mater.* **2007**, *17*, 1163.
- (11) Lloyd, M.T., Mayer, A.C., Subramanian, S., Mourey, D.A., Herman, D.J., Bapat, A.V., Anthony, J.E., Malliaras, G. G. *J. Am. Chem. Soc.* **2007**, *129*, 9144.
- (12) Rousseau, T., Cravino, A., Bura, T., Ulrich, G., Ziesse, R., Roncali, J. *Chem. Commun.* **2009**, 1673.
- (13) Bura, T., Leclerc, N., Fall, S., Lévesque, P., Heiser, T., Retailleau, P., Rihm, S., Mirloup, A., Ziesse, R. *J. Am. Chem. Soc.* **2012**, *134*, 17404.
- (14) Silvestri, F., Irwin, M.D., Beverina, L., Facchetti, A., Pagani, G.A., Marks, T.J. *J. Am. Chem. Soc.* **2008**, *130*, 17640.
- (15) Mayerhöffer, U., Deing, K., Groß, K., Braunschweig, H., Meerholz, K., Würthner, F. *Angew. Chem. Int. Ed.* **2009**, *48*, 8776.
- (16) Bürckstümmer, H., Kronenberg, N. M., Gsänger, M., Stolte, M., Meerholz, K., Würthner, F. *J. Mater. Chem.* **2010**, *20*, 240.
- (17) Walker, B., Tamayo, A. B., Dang, X.-D., Zalar, P., Seo, J. H., Garcia, A., Tantiwiwat, M., Nguyen, T.-Q. *Adv. Funct. Mater.* **2009**, *19*, 3063.
- (18) Walker, B., Kim, C., Nguyen, T.-Q. *Chem. Mater.* **2011**, *23*, 470.
- (19) Mishra, A., Bäuerle, P. *Angew. Chem. Int. Ed.* **2012**, *51*, 2020.
- (20) Lin, Y., Li, Y., Zhan, X. *Chem. Soc. Rev.* **2012**, *41*, 4245.
- (21) Sun, Y., Welch, G. C., Leong, W. L., Takacs, C. J., Bazan, G. C., Heeger, A. J. *Nat. Mater.* **2012**, *11*, 44.
- (22) Eftaiha, A. F., Hill, I. G., Sun, J.-P., Welch, G. C. *J. Mater. Chem. A* **2013**, DOI: 10.1039/C3TA14236A.

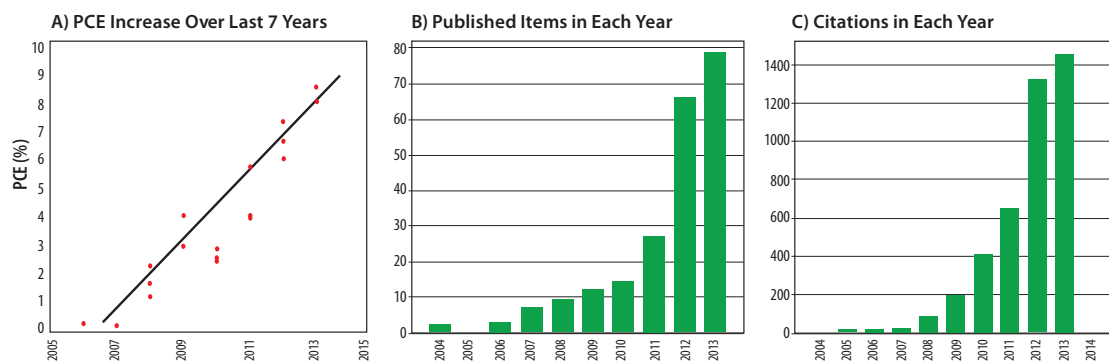


Figure 4. A) Plot of highest reported power conversion efficiencies for solution-processed small molecule solar cells from 2006 to 2013. Web of Knowledge generated reports showing B) the number of publications and C) the number of citations since 2003 for the search topic 'solution processed small molecule solar cells'.

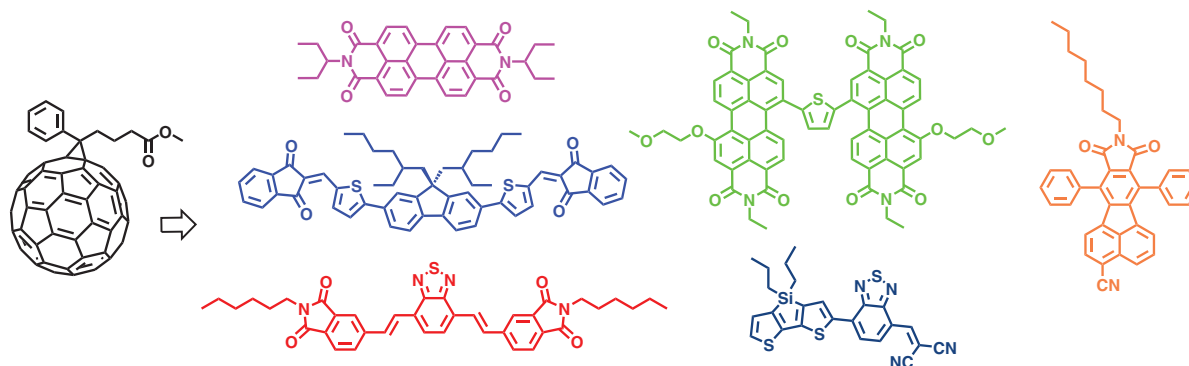
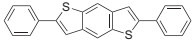
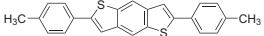
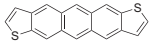
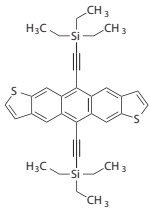
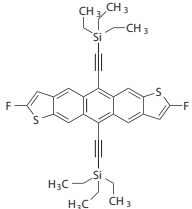
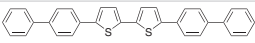
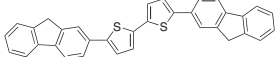
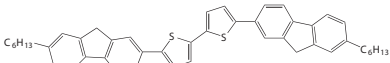
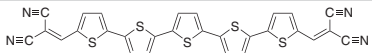
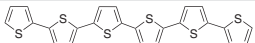
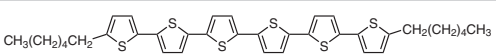
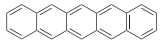
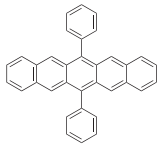
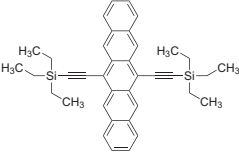


Figure 5. Example structures of linear donor-acceptor type small molecules utilized as acceptors replacing fullerene derivatives in solution-processed bulk-heterojunction solar cells.

# P-type Small Molecules

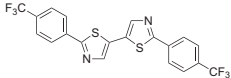
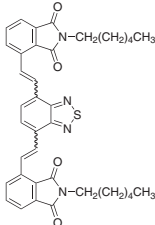
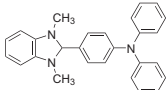
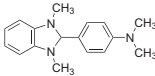
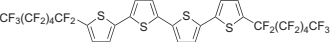
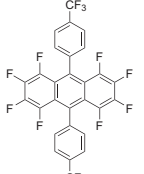
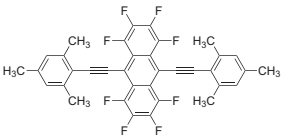
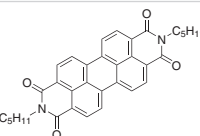
For a complete list of available materials, visit [aldrich.com/psmall](http://aldrich.com/psmall).

Structure	Name	Optical Properties/Mobility	Purity	Prod. No.
	DTS(FBTTh <sub>2</sub> ) <sub>2</sub>	$\lambda_{\text{max}}$ 590 nm in chloroform	-	772380-100MG
	DTS(PTTh <sub>2</sub> ) <sub>2</sub>	$\lambda_{\text{max}}$ 655 nm in chloroform	-	772372-100MG
	2-[[7-(5- <i>N,N</i> -Diethylaminothiophen-2-yl)-2,1,3-benzothiazol-4-yl]methylene]malononitrile	$\lambda_{\text{abs}}$ 662-664 nm in dichloromethane	99%, HPLC	777293-250MG
	2-[[7-(4-Diphenylaminophenyl)-2,1,3-benzothiazol-4-yl]methylene]propanedinitrile	$\lambda_{\text{max}}$ 549 nm in dichloromethane	96%	790524-100MG
	2-[[7-(4-[ <i>N,N</i> -Bis(4-methylphenyl)amino]phenyl)-2,1,3-benzothiazol-4-yl]methylene]propanedinitrile	$\lambda_{\text{abs}}$ 570 nm in dichloromethane	97%, HPLC	777048-500MG
	SMDPPEH	$\lambda_{\text{abs}}$ 644 nm in methylene chloride $\sim 10^{-4}$ cm <sup>2</sup> /V·s	97%, HPLC	753912-250MG
	SMDPPO	$\lambda_{\text{abs}}$ 644 nm in methylene chloride	-	753920-250MG
	2,4-Bis[4-( <i>N,N</i> -diphenylamino)-2,6-dihydroxyphenyl]squaraine	$\lambda_{\text{max}}$ 720 nm	98%	757233-1G
	2,4-Bis[4-( <i>N,N</i> -dibenzylamino)-2,6-dihydroxyphenyl]squaraine	$\lambda_{\text{max}}$ 640-646 nm in chloroform	97%	757268-1G
	2,4-Bis[4-( <i>N,N</i> -diisobutylamino)-2,6-dihydroxyphenyl]squaraine	$\lambda_{\text{max}}$ 700 nm	97%	758337-1G
	Dinaphtho[2,3- <i>b</i> :2',3'- <i>f</i> ]thieno[3,2- <i>b</i> ]thiophene	2 cm <sup>2</sup> /V·s	99%, sublimed grade	767638-100MG 767638-500MG
	2,7-Diphenyl[1]benzothieno[3,2- <i>b</i> ][1]benzothiophene	2 cm <sup>2</sup> /V·s	99%, sublimed grade	767603-100MG 767603-500MG

Structure	Name	Optical Properties/Mobility	Purity	Prod. No.
	2,6-Diphenylbenzo[1,2-b:4,5-b']dithiophene	$4.6 \times 10^{-3} \text{ cm}^2/\text{V}\cdot\text{s}$	97%, sublimed grade	767611-100MG 767611-500MG
	2,6-Ditolybenzo[1,2-b:4,5-b']dithiophene	$10^{-2} \text{ cm}^2/\text{V}\cdot\text{s}$	95%, sublimed grade	767646-100MG 767646-500MG
	Naphtho[1,2-b:5,6-b']dithiophene	$>0.5 \text{ cm}^2/\text{V}\cdot\text{s}$	97%	768677-500MG
	ADT	$0.3 \text{ cm}^2/\text{V}\cdot\text{s}$	97%	754080-250MG
	TES-ADT	$1 \text{ cm}^2/\text{V}\cdot\text{s}$	>99%, HPLC	754102-100MG
	diF-TES-ADT	$1 \text{ cm}^2/\text{V}\cdot\text{s}$	99%, HPLC	754099-100MG
	5,5'-Di(4-biphenyl)-2,2'-bithiophene	$0.04 \text{ cm}^2/\text{V}\cdot\text{s}$	97%	695947-1G
	FTF	$0.3 \text{ cm}^2/\text{V}\cdot\text{s}$	sublimed grade	754056-250MG
	DH-FTF	$0.05\text{-}0.12 \text{ cm}^2/\text{V}\cdot\text{s}$	95%	754064-250MG
	5,5''-Bis(2''''-dicyanovinyl)-2,2':5':2'':5'':2''-quinque thiophene (DCV5T)	$\lambda_{\text{abs}} 530 \text{ nm}$ in DMSO	$\geq 97\%$	745596-250MG
	$\alpha$ -Sexithiophene	$0.075 \text{ cm}^2/\text{V}\cdot\text{s}$	-	594687-1G
	5,5''-Dihexyl-2,2':5':2'':5'':2''-sexithiophene	$0.13 \text{ cm}^2/\text{V}\cdot\text{s}$	-	633216-500MG
	Pentacene	$0.4\text{-}3 \text{ cm}^2/\text{V}\cdot\text{s}$	$\geq 99.995\%$ trace metals basis, triple-sublimed grade	698423-500MG
	Pentacene	$0.4\text{-}3 \text{ cm}^2/\text{V}\cdot\text{s}$	$\geq 99.9\%$ trace metals basis, sublimed grade	684848-1G
	Pentacene	$0.4\text{-}3 \text{ cm}^2/\text{V}\cdot\text{s}$	99%	P1802-100MG P1802-1G P1802-5G
	6,13-Diphenylpentacene	UV absorption 308 nm in dichloromethane $8 \times 10^{-3} \text{ cm}^2/\text{V}\cdot\text{s}$	98%	760641-1G
	6,13-Bis(triethylsilyl)ethynylpentacene	$10^{-5} \text{ cm}^2/\text{V}\cdot\text{s}$	$\geq 99\%$ , HPLC	739278-100MG 739278-500MG

# N-type Small Molecules

For a complete list of available materials, visit [aldrich.com/nsmall](http://aldrich.com/nsmall).

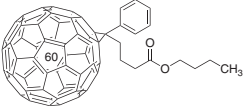
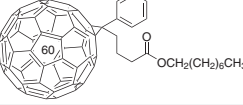
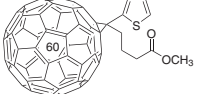
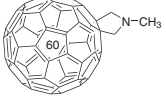
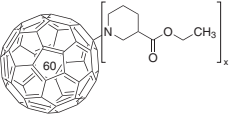
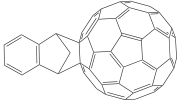
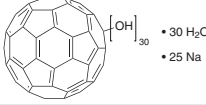
Structure	Name	Optical Properties/Mobility	Purity/Dye Content	Prod. No.
	2,2'-Bis[4-(trifluoromethyl)phenyl]-5,5'-bithiazole	1.83 cm <sup>2</sup> /Vs	97%	749257-500MG
	PI-BT	λ <sub>max</sub> 448 nm in THF	>97%	790893-250MG 790893-1G
	4-(1,3-Dimethyl-2,3-dihydro-1H-benzoimidazol-2-yl)-N,N-diphenylaniline	λ <sub>abs</sub> 308 nm in dichloromethane	98%	763721-1G
	4-(2,3-Dihydro-1,3-dimethyl-1H-benzimidazol-2-yl)-N,N-dimethylbenzenamine	-	98%, HPLC	776734-1G
	5,5''-Bis(tridecafluorohexyl)-2,2':5,2'';5',2'''-quaterthiophene	≤0.64 cm <sup>2</sup> /Vs	-	764639-250MG 764639-1G
	1,2,3,4,5,6,7,8-Octafluoro-9,10-bis[4-(trifluoromethyl)phenyl]anthracene	-	97%	757179-1G
	1,2,3,4,5,6,7,8-Octafluoro-9,10-bis[2-(2,4,6-trimethylphenyl)ethynyl]anthracene	-	97%	758442-250MG
	2,7-Dihexylbenzo[1,3,8]phenanthroline-1,3,6,8(2H,7H)-tetrone	λ <sub>abs</sub> 380, 360, 342 nm in dichloromethane, 0.7 cm <sup>2</sup> /Vs	-	768464-500MG
	1,3,6,8(2H,7H)-Tetraone, 2,7-dicyclohexylbenzo[1,3,8]phenanthroline	λ <sub>abs</sub> 382, 362, 243 nm in chloroform, 6 cm <sup>2</sup> /Vs	98%	761443-1G
	N,N-Dimethyl-3,4,9,10-perylenedicarboximide	λ <sub>abs</sub> 522 nm in dichloromethane, 10 <sup>3</sup> cm <sup>2</sup> /Vs	98%	771481-1G 771481-5G
	2,9-Dipropylanthra[2,1,9-def,6,5,10-d'ef']diisoquinoline-1,3,8,10(2H,9H)tetrone	λ <sub>abs</sub> 524, 488 nm, 0.1-2.1 cm <sup>2</sup> /Vs	97%	771635-1G
	N,N'-Bis(3-pentyl)perylene-3,4,9,10-bis(dicarboximide)	λ <sub>abs</sub> 524, 488, 457 nm in dichloromethane	99%, HPLC	776289-1G
	N,N-Dipentyl-3,4,9,10-perylenedicarboximide	λ <sub>max</sub> 527 nm, ~10 <sup>-4</sup> cm <sup>2</sup> /Vs	98%	663921-500MG
	2,9-Dihexylanthra[2,1,9-def,6,5,10-d'ef']diisoquinoline-1,3,8,10(2H,9H)tetrone	λ <sub>abs</sub> 524, 448, 229 nm in dichloromethane, 0.1-2.1 cm <sup>2</sup> /Vs	98%	773816-1G

Structure	Name	Optical Properties/Mobility	Purity/Dye Content	Prod. No.
	2,9-Diheptylanthra[2,1,9-def,6,5,10-d'e'f']diisoquinoline-1,3,8,10(2H,9H)tetrone	$\lambda_{\max}$ 254 nm in dichloromethane, $1.4 \times 10^{-2}$ cm <sup>2</sup> /V-s	99%	773824-1G
	N,N'-Dioctyl-3,4,9,10-perylenedicarboximide	$\lambda_{\max}$ 526 nm, $1.7$ cm <sup>2</sup> /V-s	98%	663913-1G
	N,N'-Diphenyl-3,4,9,10-perylenedicarboximide	$\lambda_{\max}$ 527 nm, $10^{-3}$ cm <sup>2</sup> /V-s	98%	663905-500MG
	N,N'-Bis(2,5-di-tert-butylphenyl)-3,4,9,10-perylenedicarboximide	$\lambda_{\max}$ 528 nm, $1.8 \times 10^{-4}$ cm <sup>2</sup> /V-s	Dye content 97%	264229-100MG
	2,9-Bis[(4-methoxyphenyl)methyl]anthra[2,1,9-def,6,5,10-d'e'f']diisoquinoline-1,3,8,10(2H,9H)tetrone	$\lambda_{\text{abs}}$ 527, 490 nm in dichloromethane, $0.5$ cm <sup>2</sup> /V-s	99%	771627-1G
	1,3,8,10(2H,9H)-Tetraone, 2,9-bis(2-phenylethyl)anthra[2,1,9-def,6,5,10-d'e'f']diisoquinoline	$1.4$ cm <sup>2</sup> /V-s	98%, elemental analysis	761451-1G
	2,9-Bis[2-(4-fluorophenyl)ethyl]anthra[2,1,9-def,6,5,10-d'e'f']diisoquinoline-1,3,8,10(2H,9H)tetrone	-	95%	763942-1G
	2,9-Bis[2-(4-chlorophenyl)ethyl]anthra[2,1,9-def,6,5,10-d'e'f']diisoquinoline-1,3,8,10(2H,9H)tetrone	-	98%	767468-1G

## Fullerenes

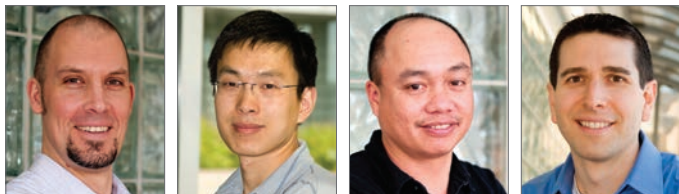
For a complete list of available materials, visit [aldrich.com/oel](http://aldrich.com/oel).

Structure	Name	Purity	Prod. No.
	[6,6]-Phenyl C <sub>71</sub> butyric acid methyl ester, mixture of isomers	99%	684465-100MG 684465-500MG
	[6,6]-Phenyl C <sub>60</sub> butyric acid methyl ester	>99.9%	684457-100MG
	[6,6]-Phenyl C <sub>60</sub> butyric acid methyl ester	>99.5%	684449-100MG 684449-500MG
	[6,6]-Phenyl C <sub>60</sub> butyric acid methyl ester	>99%	684430-1G
	[6,6]-Pentadeuterophenyl C <sub>60</sub> butyric acid methyl ester	99.5%	684503-100MG
	[6,6] Diphenyl C <sub>60</sub> bis(butyric acid methyl ester) (mixture of isomers)	99.5%	704326-100MG

Structure	Name	Purity	Prod. No.
	[6,6]-Phenyl-C <sub>61</sub> butyric acid butyl ester	>97%	685321-100MG 685321-1G
	[6,6]-Phenyl-C <sub>61</sub> butyric acid octyl ester	≥99%	684481-100MG
	[6,6]-Thienyl C <sub>61</sub> butyric acid methyl ester	≥99%	688215-100MG
	N-Methylfulleropyrrolidine	99%, HPLC	668184-100MG
	Small gap fullerene-ethyl nipecotate	≥95%, fullerenes 50%	707473-250MG
	ICMA	97%, HPLC	753947-250MG
	ICBA	99%, HPLC	753955-250MG
	Polyhydroxy small gap fullerenes, hydrated	Polyhydroxy SGFs(TGA) ~ 85%	707481-100MG

# HIGH-PERFORMANCE SEMICONDUCTOR POLYMERS

## BASED ON DIKETOPYRROLOPYRROLE AND THIENOTHIOPHENE



Tony Wigglesworth, Yiliang Wu, Cuong Vong and Matthew Heuft  
Xerox Research Centre of Canada, Mississauga ON, L5K 2L1  
Email: tony.wigglesworth@xrc.xerox.com

### Introduction

The development of high-performance conjugated organic molecules and polymers has received widespread attention in industrial and academic research. This widespread interest is motivated by the numerous applications for these materials in optoelectronic devices such as organic light emitting diodes (OLEDs),<sup>1</sup> organic field-effect transistors (OFETs),<sup>2</sup> sensors,<sup>3</sup> and organic photovoltaic (OPV) devices.<sup>2</sup> Compared to their inorganic counterparts, organic materials offer unique advantages, such as lightweight, solubility, and compatibility with flexible substrates so they can be fabricated into electronic devices using low-cost printing techniques.

Diketopyrrolopyrrole (DPP)-based materials have emerged as one of the most promising material platforms for developing high-performance polymers for printed electronics applications.<sup>4</sup> DPP polymers have excellent aggregating properties due to the strong donor-acceptor interactions induced by the electron-deficient DPP chromophore. This has led to record-breaking *p*-type mobilities of 5–10 cm<sup>2</sup>V<sup>-1</sup>s<sup>-1</sup> for polymer-based, solution-processed OFETs.<sup>5,6</sup> This versatile class of semiconductor polymers has also been utilized in bulk hetero-junction solar cells with [C60]PCBM (Aldrich Prod. Nos. 684457, 684449, and 684430) and [C70]PCBM (Aldrich Prod. No. 684465) acceptors and photoconversion efficiencies (PCE) ranging from 3–7% have been demonstrated.<sup>7</sup>

Among the numerous DPP-based materials that have been investigated, diketopyrrolopyrrole-thienothiophene (DPP-TT) copolymers have emerged as one of the most promising *p*-type organic semiconductor polymers developed in recent years. This article highlights the applications of DPP-TT copolymers in solution-processed OFET devices.

### Solution-processed Organic Field-effect Transistors

DPP-TT copolymers are soluble in common organic solvents such as chloroform, chlorobenzene, dichlorobenzene, and xylene for fabrication of OFET devices using solution processing. DPP-TT copolymer **P1** (Aldrich Prod. No. 791989) has been extensively studied due to the excellent performance in both OFET and OPV devices. For example, this DPP-based polymer has been discussed in several publications with the reported mobility ranging from 1–10 cm<sup>2</sup>V<sup>-1</sup>s<sup>-1</sup> depending on the polymer molecular weight and the device architecture.<sup>6,8</sup> Li *et al.* demonstrated a benchmark performance of 10 cm<sup>2</sup>V<sup>-1</sup>s<sup>-1</sup> in a solution-processed organic thin film transistor (OTFT) with polymer **P1**.<sup>6</sup> This outstanding performance is driven by the high molecular weight (*M<sub>w</sub>*=501 kDa) polymer attained in this example. However, despite this remarkable device performance, DPP-based polymers are predominantly processed from halogenated organic solvents which prohibit their use in large-scale commercial applications. In this report, we demonstrate that DPP-TT transistors with performance approaching 1 cm<sup>2</sup>V<sup>-1</sup>s<sup>-1</sup> can be fabricated from non-halogenated aromatic solvents under ambient conditions. We found that polymer **P1** with a weight average molecular weight of *M<sub>w</sub>*=35–50 kDa has excellent solubility in xylene solvents and investigated the device performance in solution processed OFETs.

### Device Fabrication

Top-gate bottom-contact OFETs were prepared on *n*-doped silicon wafers with a 200 nm native oxide layer. The SiO<sub>2</sub> dielectric layer was modified with an octyltrichlorosilane (OTS) (Aldrich Prod. No. 235725) or an octadecyltrichlorosilane (ODTS) (Aldrich Prod. No. 104817) self-assembled monolayer (SAM) by immersing plasma cleaned substrates in a 0.1 M toluene solution at 60 °C for 20 and 40 minutes, respectively. After silane modification, the wafers were thoroughly cleaned with toluene and isopropanol. The semiconductor layer was prepared by saturating the substrate with a 0.7 wt% *p*-Xylene solution of polymer **P1**. The solution was allowed to stand on the substrate for 2 minutes and spun at 1,000 rpm for 60 seconds, forming a uniform 25–50 nm thick film of polymer **P1**. The film was vacuum-dried at 80 °C for 10 minutes and annealed at 140 °C in vacuum. 90 μm channel devices were fabricated by vacuum-evaporating 60 nm gold electrodes through a shadow mask and the device performance was characterized using a Keithley SCS-4200 system. The polymer chemical structure, device architecture, and typical source-drain curves are shown in Figure 1.

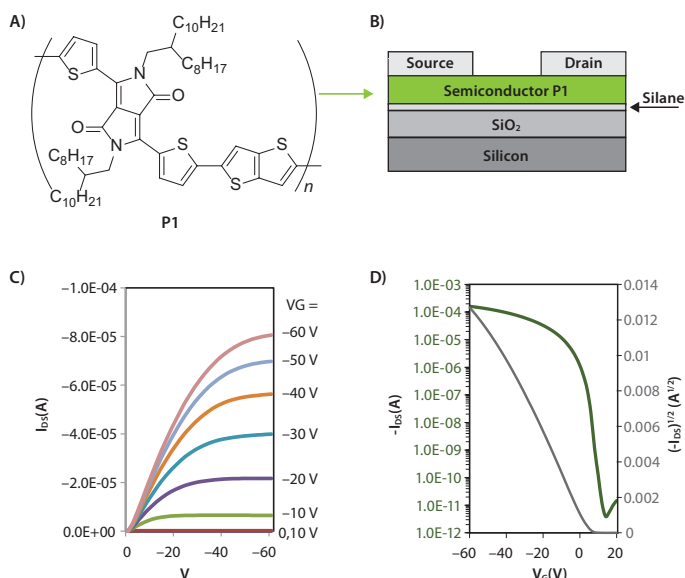


**Figure 1.** A) Chemical structure of DPP-TT. B) Top-Contact Bottom-Gate (TCBG) device architecture. C) Output curves of a typical DPP-TT transistor. D) Typical transfer curves of TCBG ( $L = 90 \mu\text{m}$  and  $W = 1,000 \mu\text{m}$ ) OTFT devices.

For  $90 \mu\text{m}$  channel devices the average saturated  $p$ -type mobility of a spin-coated device on octyltrichlorosilane (OTS) modified  $\text{SiO}_2$  dielectric was  $0.60 \pm 0.07 \text{ cm}^2\text{V}^{-1}\text{s}^{-1}$ . Devices fabricated on ODTS-modified silicon substrates further improved the average saturated mobility to  $0.96 \pm 0.08 \text{ cm}^2\text{V}^{-1}\text{s}^{-1}$ , with some devices reaching a maximum mobility of  $1.02 \text{ cm}^2\text{V}^{-1}\text{s}^{-1}$ .

## P-type Polymers

For a complete list of available materials, visit [aldrich.com/ppoly](http://aldrich.com/ppoly).

Structure	Name	Molecular Weight	Optical Properties/Mobility	Prod. No.
	PDPP2T-TT-OD	$M_w$ 40000-60000	$\lambda_{\text{max}}$ 820 nm $0.8 \text{ cm}^2/\text{V}\cdot\text{s}$	791989-100G
	PTB7	average $M_w$ 80,000-200,000	$\lambda_{\text{max}}$ 680 nm	772410-100MG
	PBDDTT-CF	-	$7 \times 10^{-4} \text{ cm}^2/\text{V}\cdot\text{s}$	772402-100MG
	Poly[(5,6-dihydro-5-octyl-4,6-dioxo-4H-thieno[3,4-c]pyrrole-1,3-diy)] [4,8-bis([2-ethylhexyl]oxy)benzo[1,2-b:4,5-b']dithiophene-2,6-diy]]	-	$\lambda_{\text{max}}$ 627 nm	773514-100MG

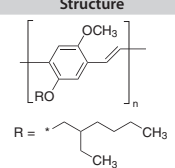
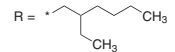
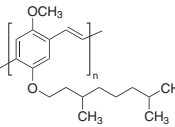
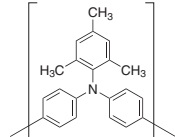
## Conclusion

Diketopyrrolopyrrole-thienothiophene (DPP-TT) copolymers are one of the most promising semiconductor materials for applications in printed electronics due to their outstanding aggregation properties provided by strong donor-acceptor interactions and solution processability. These DPP-TT copolymers have led to benchmark performance in solution-processed OFETs and OPV devices.<sup>6,7c</sup> Also, non-halogenated solvent processing has been recently demonstrated with device performance approaching the high end of amorphous silicon transistors ( $0.5\text{--}1.0 \text{ cm}^2\text{V}^{-1}\text{s}^{-1}$ ). In addition, high-performance devices can be obtained with DPP-TT copolymers at annealing temperatures of  $140 \text{ }^\circ\text{C}$ , which is compatible with low-cost plastic substrates.

## References

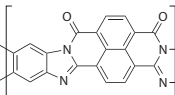
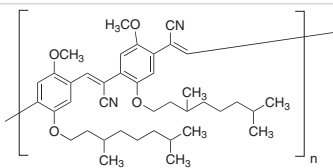
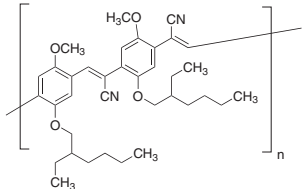
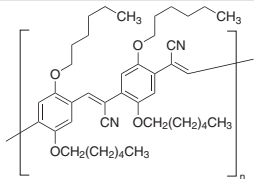
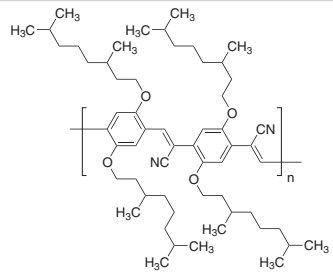
- (1) Gross, M., Müller, D.C., Nothofer, H.G., Scherf, U., Neher, D., Bräuchle, C., Meerholz, K. *Nature* **2000**, *405*, 661-665.
- (2) (a) Beaujuge, P.M. and Frechet, J.M. *J. Am. Chem. Soc.* **2011**, *133*, 20009-20029.  
(b) Mei, J., Diao, Y., Appleton, A.L., Fang, L., Bao, Z. *J. Am. Chem. Soc.* **2013**, *135*, 6724-6746.
- (3) (a) Yang, J.S. and Swager, T.S. *J. Am. Chem. Soc.* **1998**, *120*, 11864-11873.  
(b) Magliulo, M., Mallardi, A., Mulla, M.Y., Cotrone, S., Pistillo, B.R., Favia, P., Vikholm-Lundin, I., Palazzo, G., Torsi, L. *Adv. Mater.* **2013**, *25*, 2090-2094.
- (4) Nielsen, C.B., Turbiez, M., McCulloch, I. *Adv. Mater.* **2013**, *25*, 1859-1880.
- (5) Chen, H., Guo, Y., Yu, G., Zhao, Y., Zhang, J., Gao, D., Liu, H., Liu, Y. *Adv. Mater.* **2012**, *24*, 4618-4622.
- (6) Li, J., Zhao, Y., Tan, H.S., Guo, Y., Di, C.-A., Yu, G., Liu, Y., Lin, M., Lim, S.H., Zhou, Y., Su, H., Ong, B.S. *Sci. Rep.* **2**, 754; DOI:10.1038/srep00754 (2012).
- (7) (a) Bijlvel, J.C., Verstrijden, R.A.M., Wienk, M.M., Janssen, R.A. *J. Mater. Chem.*, **2011** *21*, 9224-9231.  
(b) Li, W., Roelofs, W.S.C., Wienk, M.M., Janssen, R.A. *J. Am. Chem. Soc.* **2012**, *134*, 13787-13795.  
(c) Li, W., Hendriks, K.H., Roelofs, W.S.C., Kim, Y., Wienk, M.M., Janssen, R.A. *Adv. Mater.* **2013**, *25*, 3182-3126.
- (8) (a) Li, Y., Singh, S.P., Sonar, P. *Adv. Mater.* **2010**, *22*, 4862-4866.  
(b) Zhang, X., Richter, L.J., Delongchamp, D.M., Kline, R.J., Hammond, M.R., McCulloch, I., Heeney, M., Ashraf, R.S., Smith, J.N., Anthopoulos, T.D., Schroeder, B., Geerts, Y.H., Fisher, D.A., Toney, M.F. *J. Am. Chem. Soc.* **2011**, *133*, 15073-15084.

Structure	Name	Molecular Weight	Optical Properties/Mobility	Prod. No.
	PBDTBO-TPDO	average $M_n$ 10,000-50,000	$\lambda_{abs}$ 609, 557 nm in THF	777080-100MG
	PBDT-TPD	average $M_n$ 10,000-50,000	$\lambda_{max}$ 608 nm	776300-100MG
	PBTTPD	$M_n$ 3,500-20,000	$\lambda_{em}$ 572 nm $1.0 \times 10^{-4} \text{ cm}^2/\text{Vs}$	745901-100MG
	Poly[(9,9-dioctylfluorenyl-2,7-diyl)-co-bithiophene]	average $M_n$ >20,000	$\lambda_{em}$ = 497 nm in chloroform (at $M_n$ = 20,000) $5 \times 10^{-3} \text{ cm}^2/\text{Vs}$	685070-250MG
	Poly[(9,9-di-n-octylfluorenyl-2,7-diyl)-alt-(benzo[2,1,3]thiadiazol-4,8-diyl)]	average $M_n$ 10,000-20,000	$\lambda_{em}$ = 515-535 nm in chloroform $4 \times 10^{-3} \text{ cm}^2/\text{Vs}$	698687-250MG
	PFO-DBT	average $M_w$ 10,000-50,000	$3 \times 10^{-4} \text{ cm}^2/\text{Vs}$	754013-100MG
	PSiF-DBT	$M_n$ 10,000-80,000	$10^{-3} \text{ cm}^2/\text{Vs}$	754021-100MG
	PCDTBT	average $M_w$ 20,000-100,000	$\lambda_{max}$ 576 nm $6 \times 10^{-5} \text{ cm}^2/\text{Vs}$	753998-100MG
	PCPDTBT	average $M_w$ 7,000-20,000	$\lambda_{max}$ 700 nm $2 \times 10^{-2} \text{ cm}^2/\text{Vs}$	754005-100MG
	PDTSTPD	$M_n$ 7,000	$\lambda_{max}$ 670 nm $1.0 \times 10^{-4} \text{ cm}^2/\text{Vs}$	745928-100MG
	PGeCDTPTD	$M_n$ 3,000-35,000	$\lambda_{max}$ 710 nm $0.03 \text{ cm}^2/\text{Vs}$	745936-100MG
	TQ1	$M_n$ 12,000-45,000	$\lambda_{max}$ 620 nm	745898-100MG

Structure	Name	Molecular Weight	Optical Properties/Mobility	Prod. No.
 <p>R = </p>	Poly[2-methoxy-5-(2-ethylhexyloxy)-1,4-phenylenevinylene]	average $M_n$ 40,000-70,000	$\lambda_{em} = 554$ nm in toluene	<a href="#">541443-250MG</a> <a href="#">541443-1G</a>
	Poly[2-methoxy-5-(2-ethylhexyloxy)-1,4-phenylenevinylene]	average $M_n$ 70,000-100,000	$\lambda_{em} = 554$ nm in toluene	<a href="#">541435-1G</a>
	Poly[2-methoxy-5-(2-ethylhexyloxy)-1,4-phenylenevinylene]	average $M_n$ 150,000-250,000	$\lambda_{em} = 554$ nm in toluene	<a href="#">536512-1G</a>
	Poly[2-methoxy-5-(3,7-dimethyloctyloxy)-1,4-phenylenevinylene]	$M_n \sim 120,000$	$\lambda_{em} = 555$ nm in toluene	<a href="#">546461-250MG</a> <a href="#">546461-1G</a>
	Poly[bis(4-phenyl)(2,4,6-trimethylphenyl)amine]	average $M_n$ 7,000-10,000 (GPC)	$10^{-3} - 10^{-2}$ cm <sup>2</sup> /Vs	<a href="#">702471-100MG</a> <a href="#">702471-1G</a>

## N-type Polymers

For a complete list of available materials, visit [aldrich.com/npoly](http://aldrich.com/npoly).

Structure	Name	Mobility	Prod. No.
	Poly(benzimidazobenzophenanthroline)	0.1 cm <sup>2</sup> /Vs	<a href="#">667846-250MG</a> <a href="#">667846-1G</a>
	Poly(5-(3,7-dimethyloctyloxy)-2-methoxy-cyanoterephthalylidene)	$\sim 10^{-5}$ cm <sup>2</sup> /Vs	<a href="#">646628-250MG</a>
	Poly(5-(2-ethylhexyloxy)-2-methoxy-cyanoterephthalylidene)	$\sim 10^{-5}$ cm <sup>2</sup> /Vs	<a href="#">646644-250MG</a>
	Poly(2,5-di(hexyloxy)cyanoterephthalylidene)	$\sim 10^{-5}$ cm <sup>2</sup> /Vs	<a href="#">646652-250MG</a>
	Poly(2,5-di(3,7-dimethyloctyloxy)cyanoterephthalylidene)	$\sim 10^{-5}$ cm <sup>2</sup> /Vs	<a href="#">646571-250MG</a>

# TRANSPARENT CONDUCTIVE CNT INKS

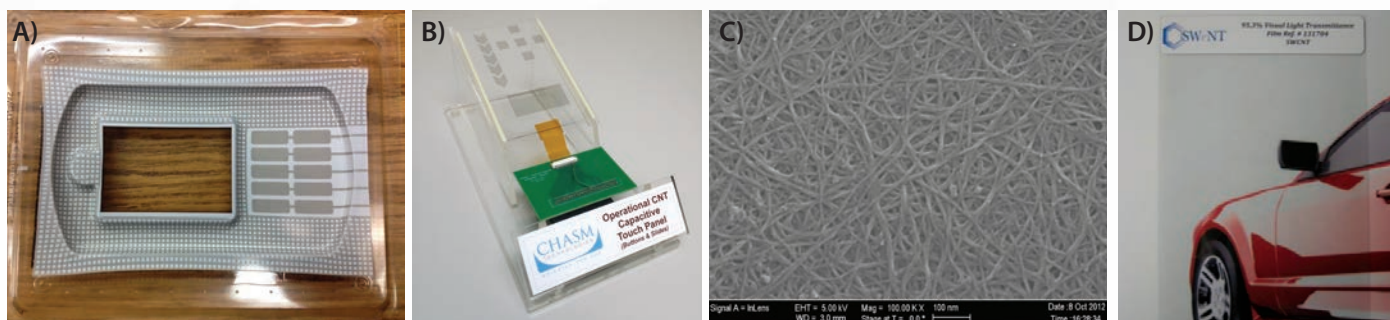
Printable • Environmentally Stable • Stretchable

Formulated using patented CoMoCAT™ CNTs, aqueous and solvent-based (V2V™) conductive inks are setting a new standard for transparent conductor performance in applications where durability and environmental stability are paramount.

## V2V™: Print. Dry. Done.

Conductive CNT Ink Systems are optimized for screen printing:

- Dries quickly, evenly at low temperature
- Contains no surfactants or electrically active dispersants, binders<sup>1</sup>
- Adheres strongly to common screen printing substrates



A) Thermoformed CNT touch sensor prototype, B) Capacitive CNT touch screen array, C) TEM scan of rod-coated CNT network (~10 mg/mm<sup>2</sup>), D) CNT TCF at 95% VLT.

## SWeNT® Conductive Inks

Description	Purpose	Sheet Resistance <sup>2</sup>			Aldrich Prod. No.	
		85% VLT	90% VLT	92% VLT		
AC100	SWCNT in aqueous surfactant solution	Spray Coating	137 Ω/sq.	237 Ω/sq.	330 Ω/sq.	791490
AC200	SWCNT in aqueous surfactant solution	Meyer-Rod/Slot-Die Coating	166 Ω/sq.	251 Ω/sq.	317 Ω/sq.	791504
VC101	SWCNT in proprietary solvent system (V2V)	Screen Printing	783 Ω/sq.	1,466 Ω/sq.	2,206 Ω/sq.	792462

1. V2V inks (e.g., VC101) contain electrically inert sulfonated tetrafluoroethylene (Nafion).

2. SR measurements for AC100, 200 taken with top coat.

For detailed product information on SWeNT® Conductive Inks, visit [aldrich.com/swnt](http://aldrich.com/swnt)



# MATERIALS TO DRIVE INNOVATION

## Across a Variety of Applications

### Energy

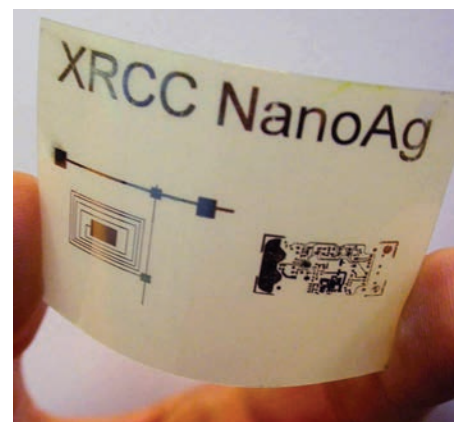
Electrode and electrolyte materials for batteries, fuel cells; hydrogen storage materials including MOFs; phosphors; thermoelectrics; nanomaterials; precursors for nanomaterials and nanocomposites

### Biomedical

Materials for drug delivery, bone and tissue engineering; PEGs, biodegradable and natural polymers; functionalized nanoparticles; block copolymers and dendrimers; and nanoclays

### Electronics

Nanowires; printed electronics inks and pastes; materials for OPV, OFET, OLED; nanodispersions; CNTs and graphene; precursors for PVD, CVD, and sputtering



Inkjet printed silver image provided by Xerox®. Aldrich® Materials Science is the proud distributor of Xerox silver nanoparticle ink.



Find more information on our capabilities at  
[aldrich.com/matsci](http://aldrich.com/matsci)